

SRM UNIVERSITY AP

Sonic Jet Injection into a Supersonic Turbulent Crossflow

Authors:

Gogula Sri Kalyan Mani Deepak
Suchet Bahadur Thapa
Sujan Bahadur Thapa

Roll number:

AP17110030005
AP17110030013
AP17110030014

Supervisor:

Dr. Satya Pramod Jammy

*Submitted in the partial fulfillment of the requirements
of the degree of Bachelor of Technology*

in the

Department of Mechanical Engineering



SRM
UNIVERSITY AP

Andhra Pradesh

Approval Sheet

This B.Tech report entitled “**Sonic Jet Injection into a Supersonic Turbulent Crossflow**” by **Gogula Sri Kalyan Mani Deepak** (AP17110030005), **Suchet Bahadur Thapa** (AP17110030013), **Sujan Bahadur Thapa** (AP17110030014) is prepared and submitted as partial fulfillment of the requirements for the degree of **Mechanical Engineering** offered by **SRM University AP**, Andhra Pradesh, India.

Examiner:



Dr Surfaraz Hussain S. Halkarni

Head Of the Department:



Dr Prakash Jadhav

Supervisor:



Dr Satya Pramod Jammy

Date: 22 May 2021

Place: Amaravati

Declaration

We, hereby declare that the final year project report entitled "**Sonic Jet Injection into a Supersonic Turbulent Crossflow**" is our original works except for quotations and citations which have been duly acknowledged. We also declare that it has not been previously or concurrently submitted for any other program at SRM University-AP, Andhra Pradesh, India, or at any other institution.

Signed:



Gogula Sri Kalyan Mani Deepak
(AP17110030005)



Suchet Bahadur Thapa
(AP17110030013)



Sujan Bahadur Thapa
(AP17110030014)

Date: 22 May 2021

Place: Amaravati

Acknowledgement

We would like to express our heartfelt thanks for the help, incentives and support we have received from all those who have given their time and shared their knowledge to make this project possible.

We would like to extend our profound gratitude to Assoc. Prof. Dr Satya Pramod Jammy, our academic advisor as well as the supervisor of this project for his continuous and immeasurable guidance, constructive comments and genuine help not only in the academic field but also in solving other problems that came up during the course of this project. He has been instrumental throughout the study period.

We would also like to extend our special thanks to the PhD. candidate, Mr Raja Mangalari for providing us with access to the DGX supercomputer and his workstation during the course of this project. His aid has been very essential for the successful completion of this project.

SRM UNIVERSITY AP

Abstract

Department of Mechanical Engineering

Bachelor of Technology

Sonic Jet Injection into a Supersonic Turbulent Crossflow

by

Gogula Sri Kalyan Mani Deepak

Suchet Bahadur Thapa

Sujan Bahadur Thapa

Shock wave boundary layer interactions (SBLI) are unavoidable physical phenomena having significant consequences in many high-speed flights and supersonic flows. Among the various categories of SBLI, transverse sonic injections into a turbulent flow involve the blockage of the supersonic flow by the secondary transverse flow resulting in the formation of strong bow shocks and wake regions while the boundary layer separates. Such shock to shock interactions in the turbulent boundary layer is the nature of SBLI interactions this work primarily focuses on. The results of Implicit Large Eddy Simulations (ILES) of SBLI are presented here to provide insights into their behaviour. The simulations are performed on a 3D flat plate with a freestream Mach number of 2.0 and an inflow Reynolds number of 500 based on the momentum thickness (θ).

The initial half of this project deals with the formation of a turbulent flow field followed by validations to evaluate the development of the turbulent boundary layer and accumulation of the time and spatial averaged flow variables. As the flow is homogeneous and set as periodic in the third dimension, the spatial averaging allows to accumulate the flow statistics and perform comparative studies with a set of selected works of literature to establish a good agreement in the generation of turbulent inflow. By implementing the synthetic turbulent method, we are able to mimic the inflow conditions as to a natural turbulent flow field. This method is fully explained by the addition of the digital factor approach.

The final part of the project involves the study and analysis of the SBLI induced in the turbulent boundary layer by subjecting the flow to a sonic injection of Mach 1. The initial effect of the injection is primarily observed by the drastic reduction in the Mach number giving rise to the wake regions. The interaction of the separated flow with the outer boundary layer illustrates the flow turning and the observation of the triple point. In essence, a detailed ILES analysis of the injection-induced SBLI reveals the formation of various complex flow structures and shock formations.

Contents

Approval Sheet	i
Declaration	ii
Acknowledgement	iii
Abstract	iv
List of Figures	vii
List of Tables	viii
List of Abbreviations	ix
List of Symbols	x
1 Introduction	1
1.1 Turbulent boundary layers and Mixing	1
1.2 Project objective	3
1.3 Project Overview	3
1.4 Summary	4
2 Literature Review	5
2.1 Shock - Wave Boundary Layer Interaction	5
2.2 OpenSBLI	9
2.3 Summary	9
3 Methodology	11
3.1 Numerical Method	11
3.1.1 Governing Equations	11
3.1.2 Discretization Schemes	12
3.2 Post Processing	13
3.2.1 Reynolds Averaging	13
3.2.2 Law of the wall	15
3.2.3 Van Driest Transformation	17
3.3 Summary	18
4 Results and Analysis	19
4.1 Flat plate turbulent boundary layer	19
4.1.1 Flat plate geometry	19
4.1.2 Mesh generation	20
4.1.3 Turbulent inflow	21
4.1.4 Numerical setup	22
4.1.5 Simulation and results	23

4.2	Injection	27
4.2.1	Injection geometry and mesh	27
4.2.2	Simulation and results	27
	Flow features	29
5	Conslusions and future work	31
5.1	Conslusions	31
5.2	Future work	31
A	OpenSBLI Coding Format	32
	Bibliography	35

List of Figures

1.1	Turbulent Boundary Layer (Mali and Dange, 2010)	2
1.2	Flow field through transverse slotted injection in supersonic crossflow (Sharma, Eswaran, and Chakraborty, 2020a)	3
2.1	Schematic of a shock-induced separation bubble (Lusher, 2020)	5
2.2	Examples of four scenarios in which shock-wave/boundary-layer interactions can occur (Babinsky and Harvey, 2011)	6
2.3	Four main steps for generating and running a simulation code in OpenSBLI (Lusher, Jammy, and Sandham, 2020)	9
3.1	Turbulent velocity fluctuations (White and Corfield, 2006)	14
3.2	Composite regions of turbulent boundary layer (Team et al., 2013)	16
4.1	Schematic diagram of domain	19
4.2	Mesh	20
4.3	Density contour at 9 flow-through times	22
4.4	Contour plots of instantaneous flow properties at 9 flow-through times	23
4.5	Momentum thickness along x	24
4.6	Contour plots of mean flow properties at 9 flow-through times	24
4.7	Spatial averaged flow properties at 9 flow-through times	25
4.8	Contour plots of spatial averaged flow properties at 9 flow-through times	25
4.9	Van Driest skin friction comparison	26
4.10	Log profile near the wall	26
4.11	Turbulence intensities	27
4.12	Schematic diagram of injection at bottom wall	28
4.13	Skin friction line plot at z=18	28
4.14	Skin friction contour plot at y=0 plane	29
4.15	Contour plots streamwise and spanwise Reynolds stresses with injection at bottom wall	29
4.16	Contour plots of Reynolds averaged variables with injection at bottom wall	29
4.17	Complex flow structures encountered during STBLI	30

List of Tables

4.1	Numerical details for the turbulent boundary layer simulations	22
4.2	Simulation parameters for 3D supersonic turbulent boundary layer	23

List of Abbreviations

SCRAMJET	Supersonic Combustion Ramjet
CFD	Computational Fluid Dynamics
SBLI	Shock Wave Boundary Layer Interaction
STBLI	Shock Turbulent Boundary Layer Interaction
DNS	Direct Numerical Simulation
LES	Large Eddy Simulations
ILES	Implicit-Large Eddy Simulations
RANS	Reynolds Averaged Navier Stokes equations
RMS	Root Mean Square
K-S	Karman-Schoenherr
NFV	Non Oscillatory Finite-Volume
SST	Shear Stress Transport model
SA	Spalart–Allmaras model
VD	Vandirest Transformation
WENO	Weighted Essentially Non-Oscillatory
TENO	Targeted Essentially Non-Oscillatory
TVD	Total Variation Diminishing
MUSCL	Monotonic Upstream-centred Scheme for Conservation Laws
OPS	Oxford Parallel Library
MPI	Message Passing Interface
OpenMP	Open Multi-Processing
OpenCL	Open Computer Language
OpenACC	Open Accelerators
CUDA	Compute Unified Device Architecture
GPU	Graphics Processing Unit

List of Symbols

θ	Theta
α	Angle
ρ	Density
T	Temperature
T_{aw}	Adiabatic wall temperature
p	Pressure
E	Energy
M	Mach number
$u_{i,j,k}$	Velocity components
C_f	Coefficient of skin-friction
Re_∞	Freestream Reynolds number
ρ_∞	Freestream density
T_∞	Freestream temperature
u_∞	Freestream velocity
M_∞	Freestream Mach number
L_∞	Freestream length of domain
q_k	Heat flux
τ_{ij}	Stress tensor
τ_w	Surface shear stress
μ_w	Kinematic viscosity
Re	Reynolds number
Pr	Prandtl number
γ	Ratio of heat capacities
δ_r	Discrete cut -off function
C_T	Cut-off parameter
X_r	Smoothness measure
β_r	Smoothness indicator
τ_k	Global smoothness indicator
\bar{u}	Time averaged velocity
u'	Fluctuating velocity
t_0	Initial starting time
L_i	Length of domain in i-direction
N_i	Number of grid points in i-direction
b_y	Stretching factor
$c_{f,incomp}$	Compressible skin friction

Chapter 1

Introduction

“Study hard what interests you the most in the most undisciplined, irreverent, and original manner possible.”

—Richard Feynmann

This century has been able to witness the development of infrastructures and technologies at unprecedented levels in a short time and has even been able to explore fields that were once deemed to be superficial. Orville Wright's history-making flight carried him a little over 36 meters in the 12 seconds that he spent in the air at the sands of Kitty Hawk. As we mark the centenary of that flight which coincides with the demise of the world's only supersonic passenger jet, *Concorde*. Numerous efforts around the world are underway to develop aircraft that could travel a thousand times faster than the Wright Flyer. Such hypersonic vehicles could provide reliable, low-cost access to space and would also have potential military applications. However, the ultimate hypersonic promise has been to attain high-speed commercial transportation between any two locations on the planet or even beyond pushing the limits of aerodynamics (Misra, 2016).

Therefore, in recent years, turbulence has become a more lively area of scientific research and application as a deeper understanding of turbulent flows ably meets the above expectations particularly by developing both physical insight and the mathematical framework needed to animate the mentioned potentials (Pope, 2001). Compared to laminar flows, generally characterized with small scale Reynolds number and low velocities, for viscous fluids, the flows are controlled by viscous diffusion of vorticity and momentum with steady solutions to the equations of motions while in turbulent flows at large Reynolds numbers, the fluid's inertia overcomes the viscous stresses causing rapid velocity and pressure fluctuations ultimately resulting in a 3D unsteady flow field. From flow past vehicles such as rockets and aircraft to planetary boundary layers and cloud motions, virtually all flows of practical engineering applications are turbulent. Thus, any analysis of fluid motion for general applications requires turbulence interpretation and although vigorous research has been conducted to better understand the physics of turbulence, it is still considered as the major unsolved problem of classical physics (Wilcox, 2006).

1.1 Turbulent boundary layers and Mixing

The knowledge of turbulent boundary layers at high Mach numbers is one of the most important foundations for designing high-speed vehicles, as the turbulent boundary layers determine the aerodynamic drag and heat transfer. The fundamental physics of the turbulent boundary layers and their structure have been studied and addressed in literature for a while now (e.g Buffin-Bélanger, Roy, and Demers, 2013; Cousteix, 2003).

In the analysis of the turbulent boundary layer, three qualitatively distinct but overlapping regions can be recognized namely - a thin viscosity dominated region next to the boundary

called the **viscous sublayer**, turbulence dominated **outer layer** and a **buffer layer** in between as shown in figure 1.1. The viscous sublayer experiences random fluctuations in velocity as a result of the advection of eddies from regions farther away from the wall. It is important to note that because the fluctuations in velocity normal to the boundary must decrease to zero at the boundary itself, molecular transport of fluid momentum is dominant over turbulent transport of momentum near the boundary. The buffer layer, also known as the turbulence-generation layer, experiences the generation of small-scale turbulence due to the instability of the sheared flow, and there is a sharp peak in the conversion of mean-flow kinetic energy to turbulent kinetic energy, and in the dissipation of this turbulent energy as well. The outer layer occupying most of the flow depth is characterised by predominant turbulent shear stress and the viscous shear stress is neglected. Mainly, this is because of their large size, the turbulent eddies here are more efficient at transporting momentum normal to the flow direction than the smaller eddies nearer the boundary. Hence, the profile of mean velocity is also much gentler in this region than nearer the bottom.

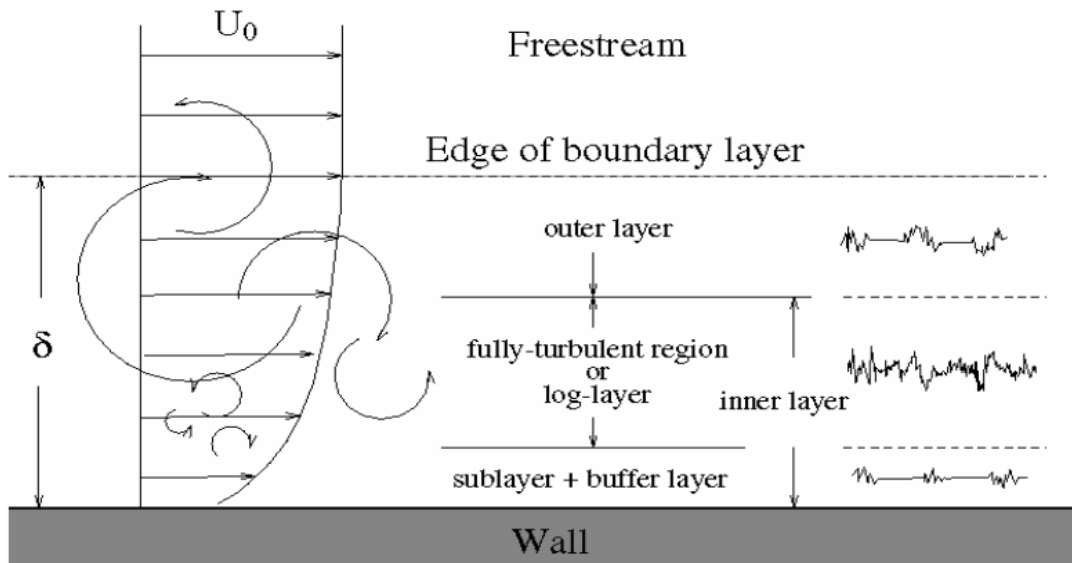


FIGURE 1.1: Turbulent Boundary Layer (Mali and Dange, 2010)

Despite the considerable progress made over the last century, perplexities yet over the correct illustration of the overlap regions be it the log or the power law, the universality of the law of the wall for various flow cases as well as the skin-friction relations. In his assessment of turbulent boundary layers, (Schlatter and Örlü, 2010) compared the statistics obtained from seven different Direct Numerical Simulations (DNS) under zero pressure gradient and addressed large differences in basic integral quantity such as the friction coefficient (c_f) and also in the predictions of mean and fluctuation profiles far into the sublayer. He reported the sensitivity of the spatial development of the flow towards inflow conditions, sufficient settling lengths and appropriate geometry dimensions responsible for such differences.

Consequently, in the recent decade, experiments with high Reynolds numbers have been considerably performed to establish sufficient scale separation and overlap region (e.g. Österlund, 1999). In addition, there has also been an increased interest in Implicit Large Eddy Simulations (ILES) where the use of specific numerical algorithms based on nonoscillatory finite-volume (NLFV) methods provides effective modelling of the unresolved dynamics of high Reynolds number fluid flows (Drikakis, 2003).

One of the extensively exploited dynamic characteristics of turbulence is its ability to effectively mix externally introduced fluids to a molecular scale having a wide range of applications under turbulence mixing in the engineering domain. Fluid entrained, or otherwise

introduced in a turbulent region, is transported and dispersed across it by motions induced from the largest to the smallest eddies, where molecular diffusion with a high Reynolds number allows slow molecular mixing to proceed effectively. For example - a recent study by (Sharma, Eswaran, and Chakraborty, 2020b) presented the effect of variation of the angle of injections in a multi-injector SCRAMJET engine using the low-Re SST and Menter's SST model on an in-house 3-D unstructured solver. He concluded an increase in the mixing volume when both the jets have the same *negative* angles of injection, specifically with -45° giving better flame-holding and enhanced mixing at no cost to thermodynamic performance.

1.2 Project objective

The purpose of the work performed in this project is primarily to attain a better understanding and provide a preferable analysis of the characteristic turbulent flow field behaviour while subjected to external fluid injection. Implicit Large Eddy Simulations (ILES) on a flat plate geometry is performed to uncover the physical aspects of this interaction as shown in figure 1.2.

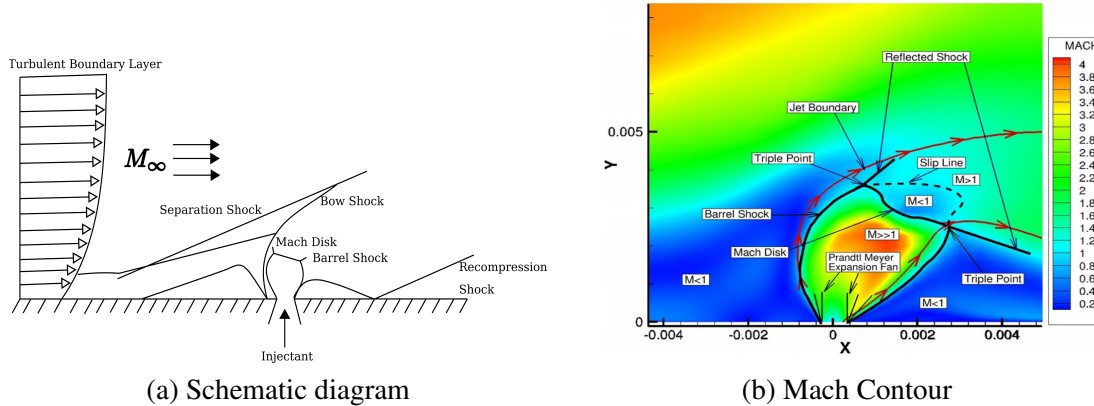


FIGURE 1.2: Flow field through transverse slotted injection in supersonic crossflow (Sharma, Eswaran, and Chakraborty, 2020a)

This can only be achieved by initially developing a detailed fundamental understanding of SBLIs, turbulent flows, their characteristics, different scales of turbulence, and turbulence modellings. Therefore, the general aim of this project can be summed up as an attempt to answer the following question -

“How does injecting a sonic jet into a supersonic turbulent fluid affect the flow features?”

The knowledge and insights learned from this work should also apply to any practical streams leading to scramjet injection studies as well as mixing effectiveness studies in scramjet combustions. This work is dominantly numerical and computational with some comparative studies carried out to provide validation data for the simulations.

1.3 Project Overview

The further discussions of the project are organized into several following chapters which are described briefly below,

Chapter 2 - literature review provides an overview of the relevant literature, to give an understanding of the current research environment in the field of shock-wave/boundary-layer interactions and turbulence modelling. Further topics investigated include assessment of shock-capturing numerical schemes, computational analysis of Transverse Sonic Injection, viscous flow fields, Vandirest wall transformations, DNS, and LES simulations. Also, a detailed study in the working of solver, OpenSBLI was performed.

Chapter 3 - Methodology this chapter presents the overview of the governing equations that have been used during the numerical simulations as well as the discretization schemes such as TENO and central differencing schemes as to how they perform shock-capturing with minimum numerical dissipation. It also introduces the post-processing concepts that justify the wall behaviours and VD transformations useful for analysis of the turbulent flow behaviour and characteristics from the outputs obtained.

Chapter 4 - Results and Analysis this chapter focuses on the generation of the most attainable realistic turbulent inflow followed with validation. The flow structures generated, accumulation of statistical flow variables are presented through simulations in both the cases of with and without sonic jet injections. Comparison studies with reference to a few selected pieces of literature were showcased. Additionally, the mixing phenomena after introducing sonic jet injections into the supersonic flow field was also demonstrated.

Chapter 5 - Conclusions and Future work The final chapter of this project summarizes the findings and analysis of the previous chapters and ties them back to the objective question posed in section 1.2. The chapter concludes by presenting a set of propositions and plans as to how the work performed on this project can be extended.

1.4 Summary

This chapter was planned to deliver the reader with elemental knowledge and the concept of turbulent boundary layers and SBLIs. The motivation for this work that follows was defined. This chapter also enclosed the basic structure of this project to answer the objective question presented. Thus, we now move on to the body of the project work which aims to provide and define the scope of the project in detail.

Chapter 2

Literature Review

The relevant concepts in a context such as SBLIs, turbulence mixing and injection studies have been a field of active study for more than a century and a substantial body of literature exists to provide the background and basis for the present work. This review aims to establish the context in which this project fits into the domain of turbulent modelling as a whole and, how it will lay out fundamental insights for the analysis of turbulent boundary layer interactions and mixing studies. As such, this chapter begins with a brief overview of the primary definitions and concepts of shock wave boundary layer interactions.

2.1 Shock - Wave Boundary Layer Interaction

Shock turbulence boundary layer interaction (STBLI) is a phenomenon that is encountered quite frequently during the design of high-speed aero vehicles along with propulsion systems and can be a critical factor in determining their performance as shown in figure 2.1. Babinsky

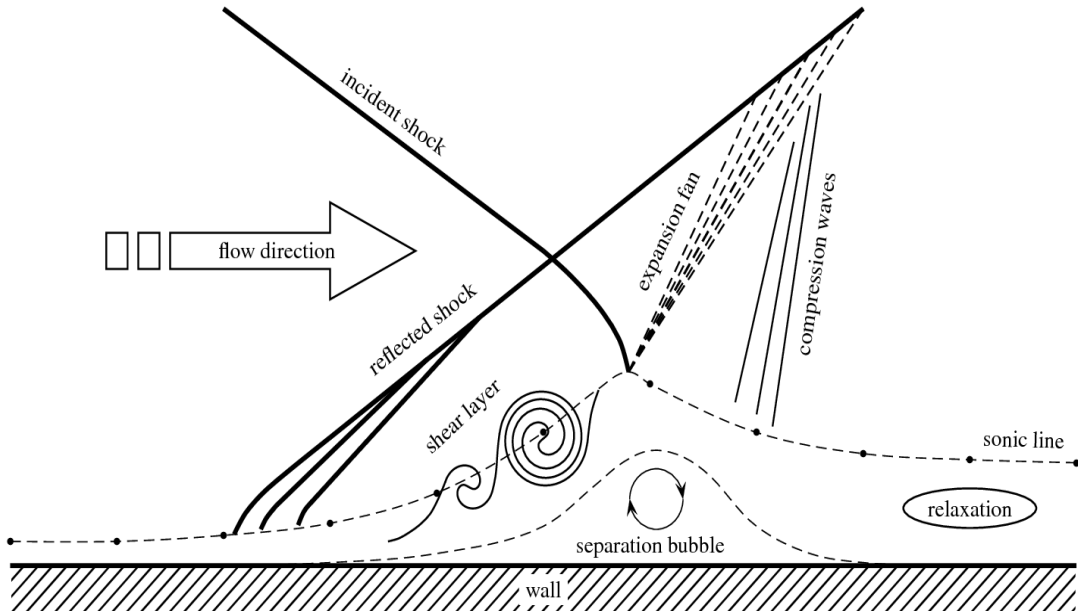


FIGURE 2.1: Schematic of a shock-induced separation bubble
(Lusher, 2020)

and Harvey (2011) and Sandham (2013) explained such interactions as inevitably complex structures as the shock must propagate through a multilayered viscous and inviscid flow structure while at the same time the boundary layer is subjected to an intense adverse pressure gradient imposed by the shock. Further, Babinsky and Harvey (2011) stated for non-laminar flows, the production of turbulence is enhanced which amplifies the viscous dissipations leading to further dramatic changes in the entire flow field in case the shock separates the

boundary layer with the formation of intense vortices or complex shock patterns that replace a relatively simple, predominantly inviscid, unseparated flow structure.

STBLIs have been a field of active study for almost a century however, there still lacked an in-depth analysis and understanding of the overall flow structures and behaviours generated in such interactions. A review issued by Dolling (2001) addressed the need for an improved understanding of unsteady shock oscillations and complex three-dimensional (3D) effects. Nevertheless, significant improvements in regards to computational power have allowed us to numerically investigate unsteady 3D STBLI effects in recent decades. Likewise, with efforts to better analyse such interactions, Babinsky and Harvey (2011) and Lusher (2020) have discussed the occurrence of SBLIs in both internal and external flow configurations and illustrated the typical scenarios where shock wave boundary layer interactions are generated, shown in figure 2.2

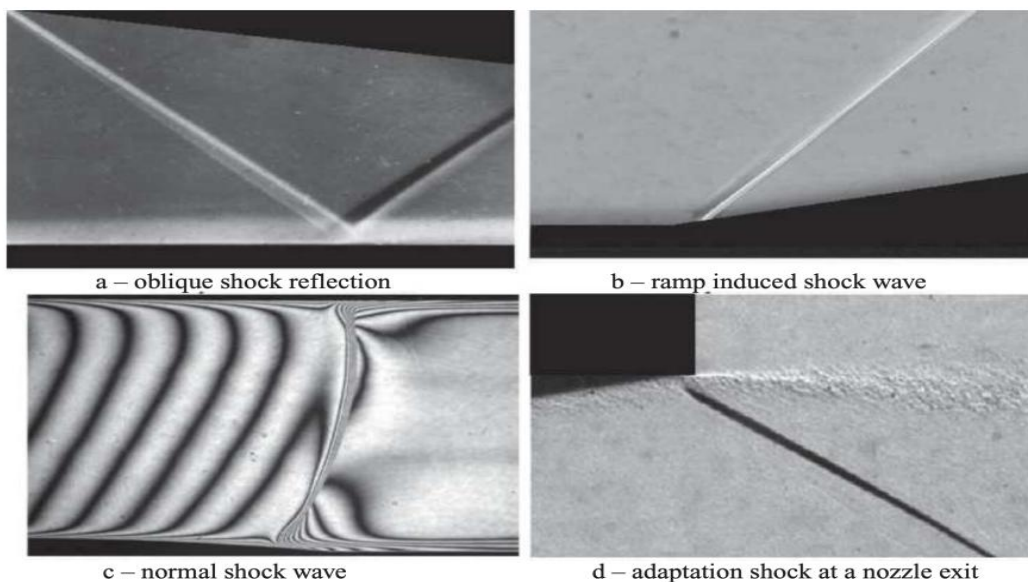


FIGURE 2.2: Examples of four scenarios in which shock-wave/boundary-layer interactions can occur (Babinsky and Harvey, 2011)

In an oblique shock reflection(figure 2.2.a), the incident shock deflects the approaching supersonic inflow and is reflected for the downstream flow to remain parallel to the wall. Such shock patterns are usually generated due to the presence of any obstacle on a nearby surface. Lusher (2020) studied such reflection of an oblique shock wave impinging on a boundary layer and additionally focused on sidewall confinement effects for three-dimensional laminar and transitional shock-wave/boundary-layer interactions (SBLI) as the incident shock is swept down the sidewall boundary-layer. A study by John (2014) investigated the Shock wave boundary Layer Interaction to understand the effect of Mach number, wall temperature, ramp angle and total temperature on upstream influence, boundary layer separation and wall heat transfer rate. For ramp flows(figure 2.2.b), the discontinuous change in the wall inclination or any sharp change in the direction of the surface results in the generation of the shock through which the incoming flow undergoes a deflection equivalent to the ramp angle. A recent example of ramp induced STBLI was presented by the study of Ritos, Kokkinakis, and Drikakis (2018) performing large-eddy simulations on a 33° compression ramp at Mach 7.2. A 9^{th} order WENO scheme was used for discretization of convection terms with a standard 2^{nd} order central differencing used for viscous terms. A high level of asymmetry in

the turbulence at the edge of the boundary layer and inside the separation bubble was concluded. Similarly, the low-frequency unsteadiness within the separated region can prove to be harmful to the aircraft performances, recent examples of numerical studies investigating the unsteadiness in SBLI includes DNS studies performed for a turbulent boundary layer over a compression ramp at Mach 2.9. It was observed that the motions of the shock and the separation point were both correlated with the motion of the point of reattachment, suggesting there is a significant downstream influence on the interaction Wu and Martin (2008). An important numerical study on laminar oblique -SBLI simulated over a flat plate for a range of Mach numbers from 1.4 to 3.4 by Katzer (1989) concluded to have matched the theoretical conclusions where the length of the separation bubble was found to be linearly dependent on the incident shock strength. However, a recent review of this study by Sansica, Sandham, and Hu (2013) examining a few of the issues with the original work via two-dimensional (2D) direct numerical simulation (DNS), noted large integration times to obtain fully converged solutions for laminar separation bubbles and that previous studies were shown to have terminated the simulations too early before the separation bubble had been allowed to fully develop.

Despite the advanced studies in STBLI in the past decades, it is to be noted that assessment of situations with arising shock wave boundary layer interactions in presence of jet injection into supersonic crossflows have not been conducted extensively (Ton et al., 1994; Lee, Jeung, and Yoon, 1997). One of the particular reasons might be the requirement of expensive computational resource, as the prediction of such complex flow field for the design of aero propulsion vehicles and systems usually rely on the Reynold Averaged Navier Stokes (RANS) for turbulence closure, Large Eddy Simulation (LES) and Direct Numerical Simulations (DNS) studies. Such studies require a large number of grid points which in turn makes the required computational resources and computing time exorbitant in such high Reynolds number flows (Sharma, Eswaran, and Chakraborty, 2020a). In the best knowledge of the present authors, the investigation of shock wave boundary layer interactions with transverse injection flow configuration has not been systematically studied in the literature. Therefore, the primary aim of this work is to study the flow structures and behaviours in such interactions via implicit large-eddy simulations with the additional aim to enhance mixing. Some recent examples include, Direct numerical simulations (DNS) carried out to study the flow features of a Mach 5 hypersonic flow over a flat plate with film cooling injection by Cerminara, Deiterding, and Sandham (2018) in both 2D and 3D hypersonic flows studied three different configurations namely, modelled blowing on the surface, simulated slots and plenum chamber. A thin film of cold fluid adjacent to the wall behind the injection location was observed with low plenum pressure while formations of vortices around the injection slots affected the upper part of the boundary layer with high plenum pressure values. For other configurations without the plenum chamber, similar patterns were observed in which the length of the cooled region downstream of the injection location were comparable between all the cases but with higher wall temperature in modelled blowing due to strong oscillations and deformation. Also, a study on the sensitivity and accuracy of various turbulence models in capturing STBLIs along with the effect of pressure ratios and slot widths on the flow development by Sharma, Eswaran, and Chakraborty (2020a) reported improved agreement with the experimental datasets for 3D simulations while suggesting that the experiment results were not close for 2D cases. Furthermore, this study was extended to investigate the effect of fuel-jet injection angle variation on the overall performance of a SCRAMJET engine Sharma, Eswaran, and Chakraborty (2020b). It was observed that positive non-zero angles of injection, in the direction of the crossflow, provided an increased thermodynamic efficiency, while the negative non-zero angles, opposing the crossflow, augmented mixing. As mixing is of paramount importance in the SCRAMJET engine, due to high speeds and low residence times, it was concluded that having the angle of fuel jet injection in the direction opposing

the incoming flow to be an optimal approach. The degree to which the injection is slanted towards the incoming flow can be decided based on the desired rate of the simultaneous penetration of the fuel into the recirculating flame-holder, which increases with increasing angle.

It is vital to be noted that the recent advances in computational power have made implicit large-eddy simulations and direct numerical simulations (DNS) a practicable tool for analysing the underlying physical mechanism in the aforementioned induced STBLIs. In modern studies, ILES has been successfully applied to complex flows due to the combination of its simplicity of implementation and computational efficiency. Furthermore, the very absence of explicit parameters promotes increased predictiveness in simulations by offering an automatic approach to modelling more general systems of equations and coupled physical processes beyond those where classical turbulence modelling theory is grounded (Lusher, 2020). The work presented by Margolin, Rider, and Grinstein (2006) combines several strategies for justifying the ILES approach for modelling the turbulent boundary layer including theoretical development, numerical analysis, relationship to conventional approaches, and quality simulations of realistic problems. A variety of different shock-capturing schemes exist to treat this issue, typically by introducing some artificial numerical dissipation to smear the shock over several grid points. The shock-capturing schemes, to address such interactions stabilize the solution by introducing artificial numerical dissipations to smear the shock over several grid points in the vicinity of flow discontinuities. However, the accuracy of capturing such interactions depend on the contrasting requirements of the applied numerical scheme Pirozzoli (2011). In the past two decades, more sophisticated methods with superior shock capturing abilities have been explored as an improvement towards the traditional approaches. Tenaud, Garnier, and Sagaut (2000) provided a comparison between the total variation diminishing (TVD), a monotonic upstream-centred scheme for conservation laws (MUSCL), and weighted essentially non-oscillatory (WENO) schemes and observed the best shock resolving performance was attained by the 5th order WENO formulation. However, a more recent study by Johnsen et al. (2010) reported excessive numerical dissipation leading to under-predictions of the shock wave interaction thus expressing standard WENO schemes unfit for resolving compressible turbulence. Consequently, a recent extension to the family of essentially non-oscillatory (ENO) schemes named Targeted Essentially non-Oscillatory (TENO) schemes was proposed by Fu, Hu, and Adams (2016). The TENO scheme acts as a compromise between the ENO and WENO approaches by sharing similar concepts but completely discards the stencils deemed to contain discontinuities while retaining as many smooth stencils as available ultimately providing significantly lower numerical dissipations. Therefore, such low dissipative TENO schemes are a significant improvement over WENO for comparable computational costs, making them better suited to DNS or ILES of compressible turbulence. Currently, the adaptive TEN06-A scheme of Fu, Hu, and Adams (2019) have shown better performance while resolving compressible turbulence on a coarser grid.

It is worth mentioning that such low dissipative and hybrid WENO/TENO shock-capturing schemes are implemented to the numerical solver used in this work, OpenSBLI finite-difference framework, for transitional and turbulent flows containing shock-waves. Current work by Lusher (2020) has investigated the accuracy of such schemes in capturing transitional SBLIs for shock-induced breakdown to turbulence with flow separation and amplification of upstream disturbances. He noted the schemes to struggle more with a transitional flat plate SBLI on coarse grids, with some schemes giving significantly larger separation bubbles than the refined solution. Nevertheless, the TENO6-A ILES was able to closely match the refined-grid skin friction and wall pressure profiles despite a factor of 12 reductions in total grid points. He also added that a further coarsening in the wall-normal direction would result in additional savings in computational cost.

2.2 OpenSBLI

The solver used for this work is a python-based modelling framework OpenSBLI, initially developed by Jacobs, Jammy, and Sandham (2017), is an open-source code-generation system for compressible fluid dynamics (CFD) which is capable of expanding a set of differential equations written in Einstein notation, and automatically generating C code that performs the finite difference approximation to obtain a solution. This C code is then targeted with the OPS library towards specific hardware backends, such as MPI/OpenMP for execution on CPUs, and CUDA/OpenCL for execution on GPUs as shown in figure 2.3.

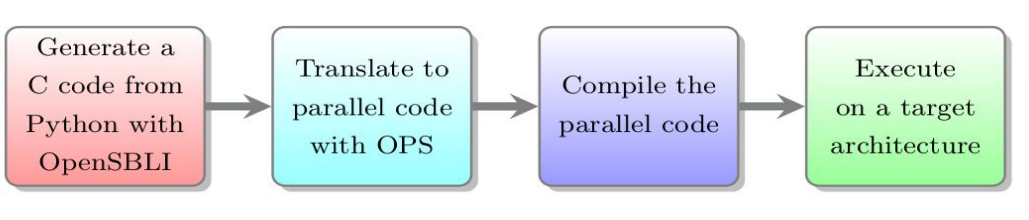


FIGURE 2.3: Four main steps for generating and running a simulation code in OpenSBLI (Lusher, Jammy, and Sandham, 2020)

The solver has also been extensively explored in the recent works by Jammy et al. (2016) and Lusher, Jammy, and Sandham (2018) in which the laminar shock-wave/boundary-layer interactions were simulated. In the work presented by Lusher, Jammy, and Sandham (2018), the code was generated with the solver using 5th order Weighted Essentially Non-oscillatory (WENO-Z) to capture shocks. It was concluded by performing runtime comparisons over different computational architectures in which the coupling of OpenSBLI to the OPS library enabled the code to run on multiple architectures from a single source code ultimately offering an efficient way of targeting emerging architectures and minimizing the development cost to the scientific researcher. The code focuses on the solution of the compressible Navier-Stokes equations with application to shock-boundary layer interactions (SBLI). However, in principle, any set of equations that can be written in Einstein notation may be solved. Using source-to-source translation the numerical solver is targeted towards different parallel hardware backends (e.g. MPI, CUDA, OpenMP, OpenCL, and OpenACC). This ensures that, for new architectures, only the backend that interfaces with the new architecture need to be written and supported by the translator Jammy et al. (2016).

Currently, a new version of this code-generation framework has been developed for compressible fluid dynamics on heterogeneous computing architectures incorporating high-order shock-capturing schemes, curvilinear coordinate transformations, and a wide range of boundary conditions shock capturing, coordinate transformations for complex geometries, and a wide range of boundary conditions, including solid walls with and without heat transfer Lusher, Jammy, and Sandham (2020). This latest version of OpenSBLI solver was shown to exhibit good weak and strong scaling on multiple GPUs, highlighting suitability for large-scale DNS as well.

2.3 Summary

It is clear that undertaking the study of turbulence and its boundary layer interactions relies upon a thorough review of fundamental research on turbulence modelling, and phenomena specific to fluid injections and mixing. In order to improve the mixing efficiency, the fundamental flow field and formation of bow shocks and Mach disks with boundary layer separations must be familiarized. Similarly, specific flow structures near the boundary wall need

to be identified and characterized to validate the wall behaviours. It should be noted that all the aforementioned studies have not only offered the general concepts on STBLI and flow features based on turbulent flow fields but the works conducted by the authors have also presented insights in improving and increasing the mixing phenomena by the effect of variation of the angle of injection, introducing multiple injections as well as through advanced computational simulations and validations. This work performs ILES with TENO and central schemes to model the turbulence and capture the STBLIs induced through a transverse injection flow configuration. The methodology by which this study was undertaken is presented in the next chapter.

Chapter 3

Methodology

This chapter showcases the shock-capturing schemes, numerical methods, and the post-processing concepts used in this work in detail. The study was numerical, employing the tools of computational fluid dynamics (CFD) to simulate the flow reactions along with the geometry. This work also involved comparative studies to provide validation data for comparison with numerical solutions referred. The methodology is presented in this section that follows, commencing with the description of fluid flow equations adopted followed by the post-processing concepts.

3.1 Numerical Method

3.1.1 Governing Equations

The governing equations used in this work for all the simulations are obtained by solving the dimensionless compressible 3D Navier Stokes equation for a Newtonian fluid. We apply the conservation of mass, momentum and energy in three spatial directions and define them as given below,

$$\frac{\partial \rho}{\partial t} + \frac{\partial(\rho u_k)}{\partial x_k} = 0 \quad (3.1)$$

$$\frac{\partial(\rho u_i)}{\partial t} + \frac{\partial(\rho u_i u_k + p \delta_{ik} - \tau_{ik})}{\partial x_k} = 0 \quad (3.2)$$

$$\frac{\partial(\rho E)}{\partial t} + \frac{\partial(\rho u_k(E + \frac{p}{\rho}) + q_k - u_i \tau_{ik})}{\partial x_k} = 0 \quad (3.3)$$

where, ρ , T , u_k are the density, temperature and the velocity components respectively. The equations are non-dimensionalized using the free stream values (ρ_∞ , T_∞ , u_∞ , M_∞ and L_∞). δ_{ik} and ∂x_k represent Kronecker delta and the cartesian coordinates respectively. The energy is defined as (E) where q_k and τ_{ij} are the heat flux and stress tensor respectively defined as,

$$q_k = \frac{-\mu}{(\gamma - 1) M_\infty^2 Pr Re} \frac{\partial T}{\partial x_k} \quad (3.4)$$

$$\tau_{ik} = \frac{\mu}{Re} \left(\frac{\partial u_i}{\partial x_k} + \frac{\partial u_k}{\partial x_i} - \frac{2}{3} \frac{\partial u_j}{\partial x_j} \delta_{ik} \right) \quad (3.5)$$

where Re , Pr and γ are defined as the Reynolds number, Prandtl number and ratio of heat capacities respectively.

The pressure is normalised by $\rho_\infty^* u_\infty^{*2}$, to give $(u_\infty, \rho_\infty, t_\infty) = 1$ in the freestream. Unless specifically stated, temperature dependent dynamic viscosity $\mu(T)$ is given by the Sutherland's

law,

$$\mu = T^{\frac{3}{2}} \left(\frac{1 + \frac{T_s}{T_\infty}}{T + \frac{T_s}{T_\infty}} \right) \quad (3.6)$$

with freestream and Sutherland temperatures taken to be $T_\infty = 288.0\text{K}$ and $T_s = 110.4\text{K}$. For a freestream Mach number (M_∞), pressure and local speed of sound are defined as,

$$p = (\gamma - 1)(\rho E - \frac{1}{2}\rho u_i u_i) = \frac{1}{\gamma M_\infty^2} \rho T \text{ and } a = \sqrt{\frac{\gamma p}{\rho}} \quad (3.7)$$

Throughout this work the wall-normal skin friction C_f is calculated as,

$$C_f = \frac{T_w}{\frac{1}{2}\rho_\infty u_\infty^2} \quad (3.8)$$

for a wall shear stress

$$T_w = \mu \frac{\partial u}{\partial y} \Big|_{y=0} \text{ or } T_w = \mu \frac{\partial u}{\partial z} \Big|_{z=0, L_z} \quad (3.9)$$

depending on whether the quality is being evaluated on the bottom wall ($y = 0$) or sidewalls ($z = 0, L_z$) of the domain.

3.1.2 Discretization Schemes

Interactions between shock waves and turbulence are ubiquitous in high-speed flows that are of practical aeronautical interest. Here, we describe the numerical schemes implemented into the compressible flow solver OpenSBLI during the project. It is to be noted that the schemes performed are within a stencil-based finite-difference framework on structured meshes. Furthermore, the use of structured body-fitted meshes allows for the use of high-order accurate numerical methods for high-fidelity fluid simulations.

Recent reviews of the shock-capturing schemes have highlighted the necessity to reduce the numerical dissipation of the schemes at the same time retaining the ability to accurately capture shock-waves (Pirozzoli, 2011). It has been reported that resolving small scale structures in transitional and turbulent flows using shock-capturing methods introduce immoderate levels of numerical dissipation to a flow unless excessively fine grids are used. Despite the numerous attempts to reduce the numerical dissipation of underlying ENO families like WENO or improved WENO-Z schemes, a more significant improvement was instituted by the TENO schemes (Fu, Hu, and Adams, 2016).

Although the TENO and WENO scheme share the same flux reconstruction framework incorporating similar flux splitting and characteristic decompositions, the TENO scheme also has modified non-linear weights optimized for low numerical dissipation with complete removal of candidate stencils deemed to be non-smooth. The additional staggered ordering of candidate stencil is said to reduce the number of candidate stencils that are crossed by a discontinuity (Fu, Hu, and Adams, 2019), helping to enforce the underlying principles of the basic Essentially non-Oscillatory (ENO) approach. Candidate stencils that are considered smooth are included in the reconstruction with their ideal non-linear weight to further reduce numerical dissipation. For flows with low Mach numbers, standard central differencing can be applied without issue. To further improve the numerical stability, skew-symmetric formulations of the governing equations can be used with central derivatives (Lusher, 2020).

TENO scheme differs from WENO in the formulation of reformulated non-linear weights with ideal weights d_r for a scheme of order K as,

$$w_r = \frac{d_r \delta_r}{\sum_{r=0}^{K-3} d_r \delta_r} \quad (3.10)$$

where δ_r is a discrete cut-off function of the form

$$\delta_r = \begin{cases} 0 & \text{if } X_r < C_T \\ 1 & \text{otherwise} \end{cases} \quad (3.11)$$

for a tunable cut-off parameter C_T . The smoothness measures X_r here are the same as the weight normalization process in WENO

$$X_r = \frac{\gamma_r}{\sum_{r=0}^{K-3} \gamma_r} \quad (3.12)$$

comprised of the WENO-Z inspired form of non-linear TENO weights (Fu, Hu, and Adams, 2019) given by,

$$\gamma_r = C + \frac{\tau_k}{\beta_r + \epsilon})^q, r = 0, \dots, K - 3 \quad (3.13)$$

Smoothness indicators β_r are unchanged from the standard Jiang-Shu formulation (Jiang and Shu, 1996), and $\epsilon \approx 10^{-40}$ remains a small parameter to avoid division by zero. The global smoothness indicator τ_k measures smoothness over the entire stencil, and is given for the 6th order TENO scheme as,

$$\tau_6 = \left| \beta_3 - \frac{1}{6}(\beta_0 + \beta_2 + 4\beta_1) \right| \quad (3.14)$$

It is to be noted that TENO schemes are approximately (15 - 20)% computationally expensive than the WENO scheme but offer significantly lower numerical dissipation while retaining sharp shock - capturing Lusher, 2020. Consequently, the TENO scheme of 6th order with central differencing of 2nd order have been incorporated in this work.

3.2 Post Processing

3.2.1 Reynolds Averaging

It is to be known by now that the Navier Stokes equations do apply to turbulent flows. Due to the wide range of flow scales involved, actual computation of the entire velocity component $u(x, y, z, t)$ is not feasible, instead, the standard analysis of turbulence separates the fluctuating property from the time mean values. The mean velocity component and the fluctuating component can be seen in figure 3.1.a and figure 3.1.b respectively. In turbulence, the presence of random fluctuations of the various flow properties requires the use of a statistical approach in which all quantities are expressed as the sum of mean and fluctuating parts (White and Corfield, 2006; Touber, 2010). For instance, Reynolds averaging assumes a variety of forms involving either an integral or a summation, considering an instantaneous flow variable $f(x, t)$, its time average is defined as,

$$\bar{f}^t(x) = \lim_{T \rightarrow \infty} \frac{1}{T} \int_t^{t+T} f(x, t) dt \quad (3.15)$$

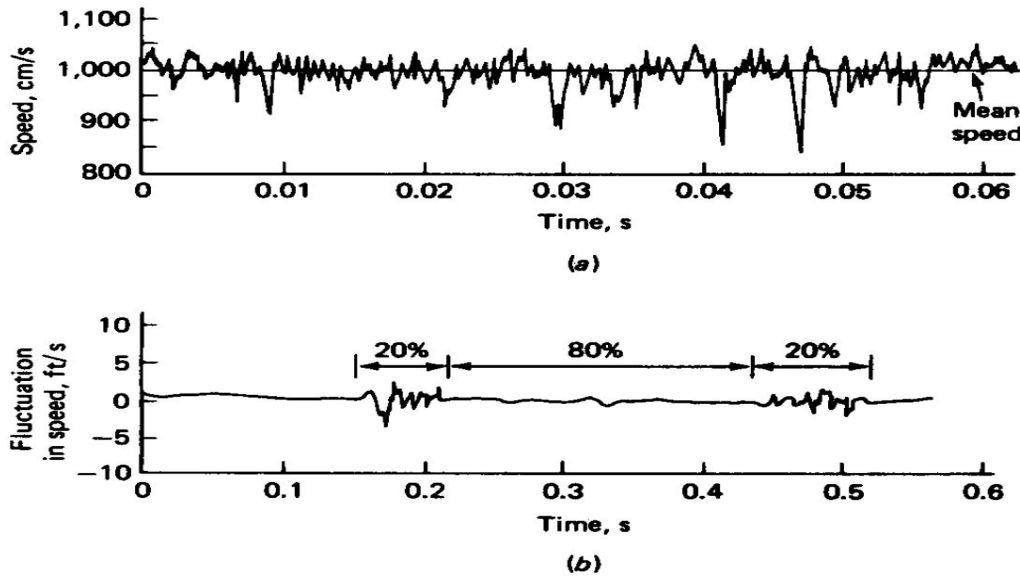


FIGURE 3.1: Turbulent velocity fluctuations (White and Corfield, 2006)

The same can be applied to a velocity profile $u(t)$ at a particular spot (x,y,z) as,

$$\bar{u} = \frac{1}{T} \int_{t_0}^{t_0+T} u dt \quad \bar{uu} = \frac{1}{T} \int_{t_0}^{t_0+T} u^2 dt \quad (3.16)$$

$$\bar{v} = \frac{1}{T} \int_{t_0}^{t_0+T} v dt \quad \bar{vv} = \frac{1}{T} \int_{t_0}^{t_0+T} v^2 dt \quad (3.17)$$

$$\bar{w} = \frac{1}{T} \int_{t_0}^{t_0+T} w dt \quad \bar{ww} = \frac{1}{T} \int_{t_0}^{t_0+T} w^2 dt \quad (3.18)$$

$$\bar{t} = \frac{1}{T} \int_{t_0}^{t_0+T} t dt \quad \bar{tt} = \frac{1}{T} \int_{t_0}^{t_0+T} t^2 dt \quad (3.19)$$

$$\bar{p} = \frac{1}{T} \int_{t_0}^{t_0+T} p dt \quad \bar{pp} = \frac{1}{T} \int_{t_0}^{t_0+T} p^2 dt \quad (3.20)$$

$$\bar{uv} = \frac{1}{T} \int_{t_0}^{t_0+T} uv dt \quad (3.21)$$

$$\bar{uw} = \frac{1}{T} \int_{t_0}^{t_0+T} uw dt \quad (3.22)$$

$$\bar{vw} = \frac{1}{T} \int_{t_0}^{t_0+T} vw dt \quad (3.23)$$

Where \bar{u} is the time average of velocity (u), t_0 is the starting time and T is the time integral which is normally chosen to be larger i.e. over a fairly large time than any significant period of the fluctuations in ' u ' mainly because mainly in failing to do so, the statistically averaged value of the scalar field at the specific location cannot be acquired. Then, the fluctuating components can be defined as,

$$\begin{aligned}
u' &= u - \bar{u} \\
v' &= v - \bar{v} \\
w' &= w - \bar{w} \\
t' &= t - \bar{t} \\
p' &= p - \bar{p}
\end{aligned} \tag{3.24}$$

By definition, it is to be noted that the mean fluctuation $\bar{u}' = 0$

Therefore, to characterize the magnitude of the fluctuation, we define and analyse its mean-square value as,

$$\overline{u'^2} = \bar{u}\bar{u} - \bar{u}^2 \tag{3.25}$$

$$\overline{v'^2} = \bar{v}\bar{v} - \bar{v}^2 \tag{3.26}$$

$$\overline{w'^2} = \bar{w}\bar{w} - \bar{w}^2 \tag{3.27}$$

$$\overline{t'^2} = \bar{t}\bar{t} - \bar{t}^2 \tag{3.28}$$

The root-mean-square value of u' is defined as $u'_{rms} = (\overline{u'^2})^{1/2}$. If the integrals above equations are independent of starting time (t_0), the fluctuations are said to be statistically stationary. The time averaging is mostly appropriate for stationary turbulence i.e. a turbulent flow that on average does not vary with time such as flow in a pipe by constant speed blower. This is because we generally adopt the statistical theory of turbulent correlation functions for turbulent flow analysis in which the statistical properties of the fluctuations: their frequency correlations, space-time correlations, and interactions with each other are studied. Further, we also emphasize the turbulent properties of relevant significance such as mean velocities and temperature profiles, wall behaviours and RMS fluctuation profiles. Accordingly, this work incorporates the concept of Reynolds time-averaging for statistical theory and numerical simulations. Applying time averaging to the basic equations of motion yields the Reynolds equations, which involve both mean and fluctuating quantities and attempts to model the fluctuation terms by relating them to mean properties or their gradients.

Additionally, the nonlinearity of the Navier Stokes leads to the appearance of momentum fluxes that act as apparent stresses throughout the flow. While deriving the equations for these stresses collection of additional unknown quantities illustrate the issue of closure i.e establishing a sufficient number of equations for all the unknowns. These additional terms cannot be neglected in any turbulent flow to calculate the mean flow properties and create analytical difficulties as their correlations are unknown. Therefore, the time-averaging procedure introduces nine new variables (a tensor component), $-\rho\bar{u}_j'\bar{u}_i'$ known as the **Reynolds-stress tensor** which can be defined only through knowledge of the detailed turbulent structure. We denote it by τ_{ij}

$$\tau_{ij} = -\overline{u_j'u_i'} \tag{3.29}$$

The spatial averaging of the 3D data has been done in the z-direction having periodic boundary condition excluding the last plane. For further discussions in Reynolds stress tensor, see (Wilcox, 2006).

3.2.2 Law of the wall

The law of the wall is a well-explored empirically determined relationship in turbulent flows near solid boundaries. Measurements have shown that for both internal and external flows, the streamwise velocity in the flow near the wall varies logarithmically with distance from

the surface, also known as the law of the wall as shown in figure 3.2. The use of empirical

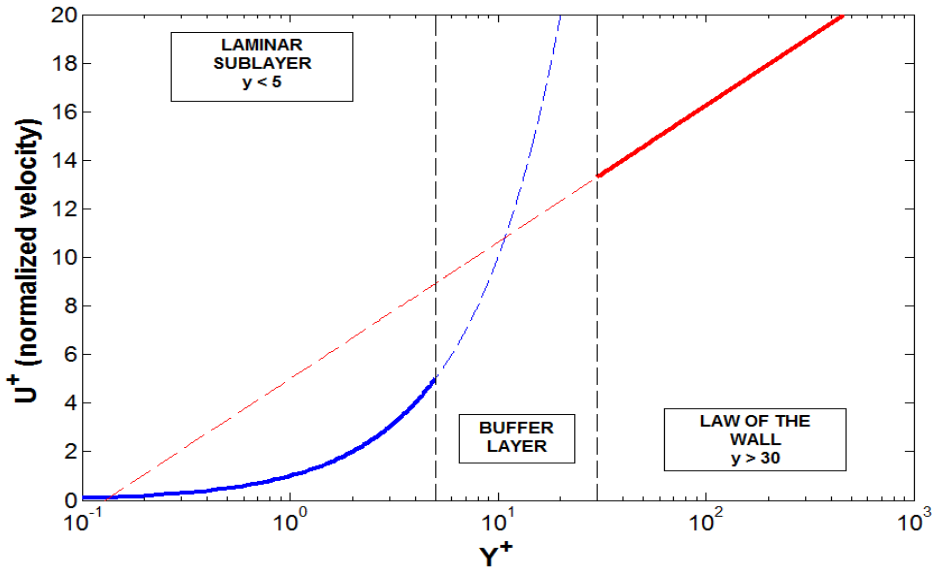


FIGURE 3.2: **Composite regions of turbulent boundary layer**
(Team et al., 2013)

functions that fits the behaviour close to the wall replacing the piece-wise linear approach with a non-linear function between the cell centroids for resolving gradients close to the wall is called wall functions. The observation of a high Reynolds number at turbulent boundary layers reveals an insignificant effect of fluid's inertia and the pressure gradient near the surface instead for dimensional analysis arguments, we use the surface shear(τ_w) stress and molecular viscosity of the fluid (μ). (DiGregorio, Drozda, and Madnia, 2019)

$$\tau_w = \mu_w \left(\frac{\partial u}{\partial y} \right)_w \quad (3.30)$$

$$\mu(T) = T^{\frac{3}{2}} \left(\frac{1 + \frac{T_s}{T_\infty}}{T + \frac{T_s}{T_\infty}} \right) \quad (3.31)$$

We can identify three distinctions namely the viscous sublayer, the log layer, and the defect layer. The log portion of the boundary layer where the sublayer and the defect layer merge i.e the law of the wall accurately representing the velocities. It is to be noted that the layers are not distinct in total but an overlap region between the inner and the outer parts of the boundary layer (Wilcox, 2006).

The standard wall functions used in this work are,

$$u^+ = \frac{u}{v^*} = \frac{u}{\sqrt{\frac{\tau_w}{\rho_w}}} \sqrt{Re_\infty} \quad (3.32)$$

$$y^+ = \frac{y v^*}{\nu_w} = \frac{y \sqrt{\frac{\tau_w}{\rho_w}}}{\nu_w} \sqrt{Re_\infty} \quad (3.33)$$

where, Re_∞ is the scaling non dimensional factor and ν_w is the free stream Reynolds number and kinematic viscosity respectively. This implementation in OpenSBLI solver can be seen in appendix A.1.

3.2.3 Van Driest Transformation

In addition to the propulsion, structural, and material challenges in hypersonic flights, some aerothermodynamic analysis techniques break down at the high speeds and rates of heat transfer encountered in hypersonic flight. A suitable example among these techniques is the law of the wall and its compressible extension, the Van Driest transformation which often fails to collapse the turbulent boundary layer velocities to a single universal profile. The logarithmic law of the wall is an empirical relationship that results from dimensional analysis and matching the velocity profiles in the viscous sublayer and the defect layer. This scaling law does allow the velocity profiles within incompressible boundary layers to be collapsed onto a single profile, thereby obtaining self-similarity. However, even though the law of the wall successfully collapses velocity profiles for incompressible flows, it does not scale velocities correctly for compressible flow. As a result, multiple attempts in extending the law of the wall to compressible flow regimes have been made in which the Vandriest transformations (VD) [I] and [II] are regarded among the most successful attempts. This is mainly because the VD transformation addresses the density variation throughout the boundary layer by transforming the mean compressible velocities to an effective incompressible velocity. It has been illustrated over the years via several DNS studies that the VD transformed velocity collapses data very well across a wide range of Mach numbers. A recent example can be seen as the Mach 47 wind tunnel test with helium of DiGregorio, Drozda, and Madnia, 2019. In the context of this work, Vandriest II transformation has been adopted for calculating the mean compressible velocities. To begin with, we define the scaled Reynolds number as Re_θ to be:

$$Re_\theta = \frac{\rho_\infty u_\infty \theta}{\mu_\infty} \quad (3.34)$$

where $\rho_\infty, u_\infty, \mu_\infty$ are the density, velocity and viscosity at the free stream. It should be noted that computation of Re_θ does involve additional postprocessing step ie. calculation of θ , defined as:

$$\theta = \int_0^\infty \rho u (1 - u) dy \quad (3.35)$$

After computing an equivalent incompressible Reynolds number Re_θ and $F_{Re\theta}$, we apply the incompressible skin-friction formula to compute $c_{f,incomp}$, by dividing the result by F_c to obtain the desired (compressible) C_f .

Using eq.3.34 we transform the compressible skin-friction to its incompressible value ($c_{f,incomp}$), is defined by the Karman-Schoenherr (K-S) relation (Schoenherr, 1932) as,

$$c_{f,incomp}(Re_\theta) = \left(17.08 (\log_{10} Re_\theta)^2 + 25.11 (\log_{10} Re_\theta) + 6.012 \right)^{-1} \quad (3.36)$$

The van Driest II transformation can be used to transform the incompressible levels to levels valid for supersonic flows with various wall temperatures. Consequently, the approximate adiabatic wall temperature is defined as,

$$T_{aw} = T_\infty \left(1 + r \frac{\gamma - 1}{2} M^2 \right) \quad (3.37)$$

where r is defined as the recovery factor set as 0.89. The compressible skin friction is related to the incompressible value in van Driest II via:

$$C_f = \frac{1}{F_c} c_{f,incomp} (Re'_\theta) \quad (3.38)$$

where,

$$Re'_\theta = Re_\theta F_{Re\theta} \quad (3.39)$$

Applying Sutherland's law, we get,

$$F_{Re\theta} = \left(\frac{1}{T_w} \right)^{3/2} \frac{T_w T_\infty + 110.4}{T_\infty + 110.4} \quad (3.40)$$

where temperatures are in $^{\circ}\text{K}$. Other correlation parameters are shown below,

$$F_c = \frac{T_{aw}-1}{(\sin^{-1} A + \sin^{-1} B)^2} \quad (3.41)$$

$$A = \frac{2a^2-b}{(b^2+4a^2)^{1/2}} \quad (3.42)$$

$$B = \frac{b}{(b^2+4a^2)^{1/2}} \quad (3.43)$$

$$a = \left(r \frac{\gamma-1}{2} M^2 \frac{T_\infty}{T_w} \right)^{1/2} = \left[(T_{aw} - 1) \frac{1}{T_w} \right]^{1/2} \quad (3.44)$$

$$b = \frac{T_{aw}}{T_w} - 1 \quad (3.45)$$

This implementation of Van Dierst transformation is applied to the OpenSBLI solver, refer appendix A.2. It is to be noted that this transformation fails to satisfactorily collapse the velocity profiles when heat transfer at the wall is introduced and is limited to cases with adiabatic wall boundary conditions Huang and Coleman, 1994. Further discussions regarding the Vandriest C_f given in eq.3.38 along with comparative studies is discussed in chapter 4.

3.3 Summary

The numerical methodology including both the numerical schemes and the post-processing has been presented, the areas in which they complement each other have also been identified. Using the aforementioned numerical schemes and discretizations, a detailed study of the shock wave boundary layer interaction with a transverse sonic injection in a supersonic crossflow configuration was carried out. The analysis begins with a detailed study of the flat plate geometry and injection configurations, which is the subject of the next chapter.

Chapter 4

Results and Analysis

In this section, turbulent shock wave boundary layer interactions (STBLI) are simulated on a flat plate adopting a random number generator for turbulent flow field development initially and extending to studies with a rectangular sonic injection flow configuration. The simulations can be viewed as an attempt to investigate the flow structures developed in the course of such complex interactions and predict the boundary layer behaviour specifically near the wall. This chapter defines the injection configurations including the details of the computational domain and the initialization of the turbulent boundary layer along with the flat plate. Furthermore, the details of modelling the mesh using the OpenSBLI solver is explained. Finally, the results obtained following the simulations are showcased.

4.1 Flat plate turbulent boundary layer

4.1.1 Flat plate geometry

While dealing with compressible turbulent boundary layers and induced shock waves, a classic problem is the compressible turbulent flow past a flat plate at arbitrary Mach number and wall temperature. Adequate studies have been presented using this setup illustrating the classic wall theories (Spalding and Chi, 1964).

The computational domain consists of a 3D flat plate with non-dimensional streamwise length, width and height set as $L_x = 640$, $L_y = 40$ and $L_z = 40$ respectively as shown in the figure 4.1. No-slip isothermal wall condition is enforced on the bottom wall with the

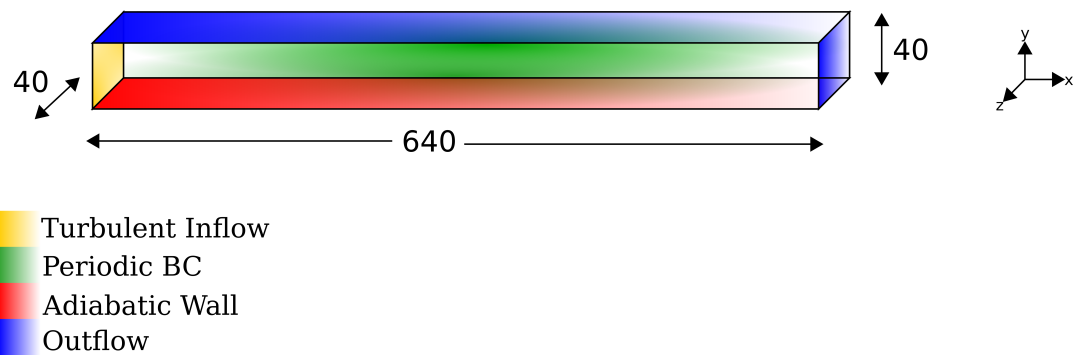


FIGURE 4.1: Schematic diagram of domain

temperature set to adiabatic wall temperature i.e. $T_{aw}/T_\infty = 1.676$. The left of the domain is initialised with a turbulent inflow while extrapolation boundary conditions applied to the top and right. A periodic boundary is enforced to the front and back of the flat plate that is

essentially in the z- dimension. A Mach 2 freestream is initialised in the domain with turbulent boundary layer profiles developed on the bottom wall of the flat plate. The freestream conditions are maintained on the top portion of the domain upstream of the boundary layer profile. The Reynolds number based on the momentum thickness (Re_θ) is taken as 500.

4.1.2 Mesh generation

The mesh is generated using OpenSBLI inbuilt generator as shown in figure 4.2. A mesh of

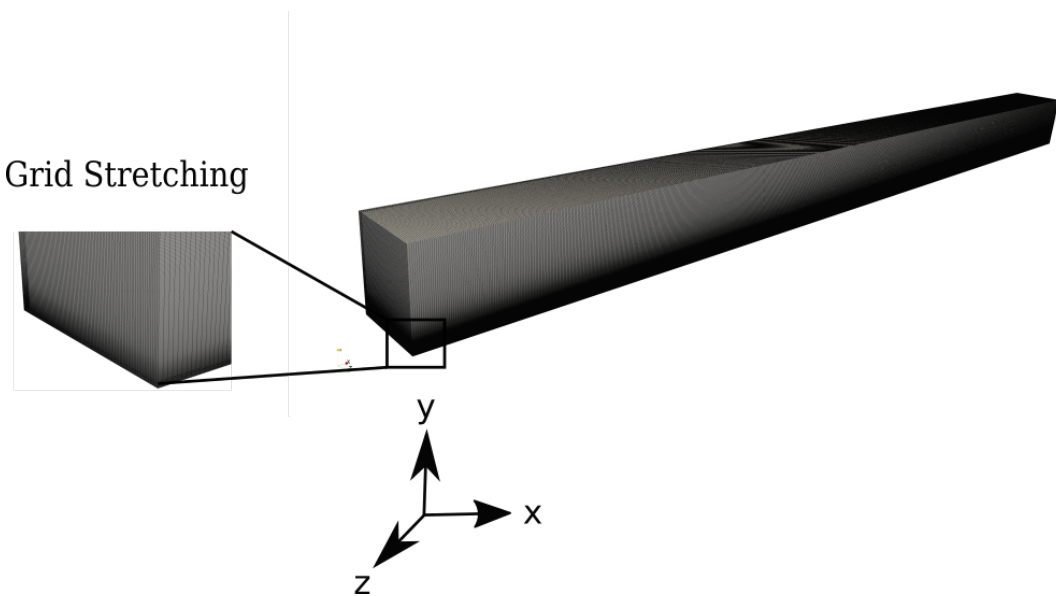


FIGURE 4.2: Mesh

size $800 \times 300 \times 90$ points in the x, y and z-directions respectively have been used. The grid is uniform in the x and z direction with stretching in the y-direction for accurate capturing of the boundary layer. Such grids provide the flexibility to use higher-order FDM numerical schemes as mentioned in chapter 2. Therefore, for this configuration, the uniformly spaced grid in x and z direction is done as,

$$x = idx \quad (4.1)$$

$$dx = \frac{L_x}{N_x-1} \quad (4.2)$$

$$z = kdz \quad (4.3)$$

$$dz = \frac{L_z}{N_z} \quad (4.4)$$

where $i = 0 \rightarrow N_x$, $k = 0 \rightarrow N_z$ are the grid indices in x and z direction respectively and N_x , N_z are the number of grid points in x and z direction.

In the y direction, the stretching is applied using an exponential function as shown below,

$$y = \frac{L_y \sinh(dy b_y \frac{j}{L_y})}{\sinh(b_y)} \quad (4.5)$$

$$dy = \frac{L_y}{N_y-1} \quad (4.6)$$

where $j = 0 \rightarrow N_y$ is the index in y-direction, N_y is the number of grid points in y-direction and $b_y = 3.0$ is the stretching factor, it is controlled in the setup script in OpenSBLI

as shown in the listing 4.1. As it is only stretched in y , it is not curvilinear so that the computational expense is controled. For further details about mesh generation refer appendix A.3.

```

1 # grid equations
2 x0 = parse_expr("Eq(DataObject(x0), block.deltas[0]*block.grid_indexes[0])
                  ", local_dict=local_dict)
3 x1 = parse_expr("Eq(DataObject(x1), Lx1*sinh(by*block.deltas[1]*block.
                  grid_indexes[1]/Lx1)/sinh(by))", local_dict=local_dict)
4 x2 = parse_expr("Eq(DataObject(x2), block.deltas[2]*block.grid_indexes[2])
                  ", local_dict=local_dict)
```

LISTING 4.1: Grid generation formula

4.1.3 Turbulent inflow

As it currently stands, the necessary key concepts and parameters for performing sonic jet injections into supersonic turbulent flow have been abundantly presented and discussed. However, when used to compute fully turbulent flows, both the LES and DNS approaches are faced with a common complexity: the necessity of prescribing realistic inflow conditions. Additionally, these conditions are ideally expected to be time and space-dependent with the correct statistical moments, phase information and spectrum of the real turbulent flow they reproduce. Practically, this is not attainable and thus one always has to deal with a certain level of approximation. Nevertheless, there are a dense number of publications reported in this issue where ultimately almost all the methods proposed to date fall under two categories namely, the precursor method and synthetic turbulence method. It is to be observed that despite the models mentioned, there does not exist any sufficiently accurate and efficient inflow generation method and that both these techniques suffer from drawbacks but moreover they attempt to provide the most realistic conditions possible (Touber, 2010). The precursor type of technique consists essentially in running an auxiliary calculation to provide the correct and targeted inflow conditions of an actual simulation. They achieve among the most realistic results (in the sense that they are the most accurate solutions) and are easy to control. It includes implementing time-dependent disturbances to the base laminar flow via wall localised blowing/suction strips to obtain intermittent transition upstream of the SBLI. A good introduction to this method can be seen in the recent work by Lusher (2020) where random phases in the forcing strip were put on to observe asymmetrical initial disturbances in the resulting SBLI structures.

This work incorporates the synthetic turbulent inflow generation method in which one prescribes an artificial inflow field that mimics real turbulence. The general idea of the method is to prescribe inflow disturbances that mimic the accepted deterministic features of turbulent boundary layers by introducing specific inner- and outer-layer disturbances representing the lifted streaks and three-dimensional vortices respectively with associated phase information.Klein, Sadiki, and Janicka, 2003 One issue in this approach is that the flow remains unphysical for some distances downstream of the inflow plane. As a consequence, it becomes inherently difficult to predict the skin-friction and displacement-thickness values downstream of this transient regime. The simplest approach to address this issue would be to insert random disturbances to the mean profiles allowing them to evolve to turbulence but this leads to relaminarization of the flow. Thus, this work adopts an alternate approach called the Digital Filter approach. This technique filters a random data field to achieve the targeted spatial and temporal correlations. In this work, the disturbances produced in the inner and outer region are an extension of an incompressible boundary layer by Sandham, Yao, and Lawal (2003) to a compressible boundary layer based on the semi-local scaling proposed by Huang, Coleman, and Bradshaw (1995). In short, the disturbances previously expressed for

an incompressible turbulent boundary layer can be simply re-scaled to the case of a compressible boundary layer. This is incorporated into the OpenSBLI solver for the turbulent inflow generation as shown in figure 4.3 From figure the visualisation of the flow can be

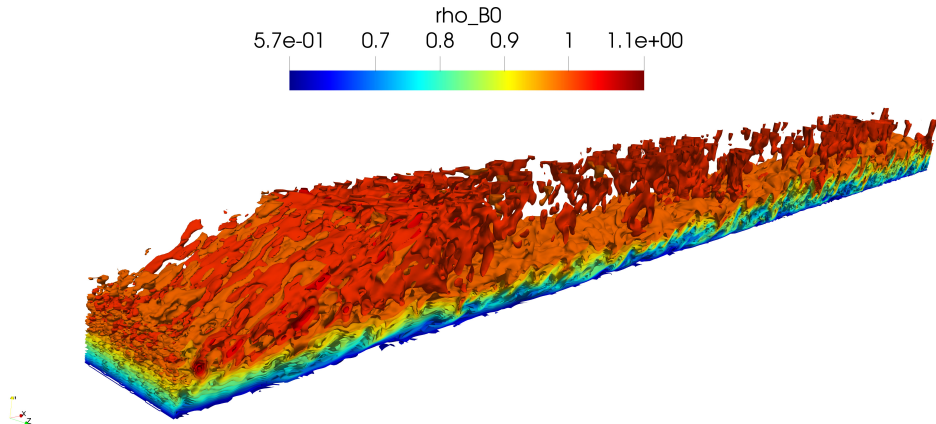


FIGURE 4.3: **Density contour at 9 flow-through times**

observed where the development of the boundary layer can be observed clearly.

4.1.4 Numerical setup

All the simulations discussed in this work have been run with a freestream Mach number of (M_∞) is 2.0 and a Reynolds number (Re_θ) is 500. The Reynolds number is set low specifically near the lower bound where the turbulence can be sustained to allow for large grid sizes while still maintaining ILES or near-ILES grid resolutions. The grid resolutions considered here referred to as ILES is summarized in table 4.1

Axis Direction		x	y	z
Domain size	L_x, L_y, L_z	640	40	40
Number of points	N_x, N_y, N_z	800	300	90
Grid resolution	$\Delta x^+, \Delta y^+, \Delta z^+$	7.5	0.43	10

TABLE 4.1: **Numerical details for the turbulent boundary layer simulations**

It is also to be observed that the grid refinement study is limited to one direction limiting the increase of computational cost of the refinement. The refinement in the wall-normal direction was performed by a stretching factor (b_y), where $b_y = 3$ as explained in section 4.1.2. Likewise, the other necessary initialization parameters used for the simulations are illustrated in table 4.2.

Quantity	Symbol	Value
Free-stream Mach number	M_∞	2.0
Reynolds Number	Re_θ	500
Reynolds number based on inlet displacement thickness	Re_δ	670
Prandtl number	Pr	0.72
Sutherland temperature	T_{suth}	110.4
Reference temperature	T_{Ref}	288.0
Non-dimensional wall temperature	T_w	1.676

TABLE 4.2: Simulation parameters for 3D supersonic turbulent boundary layer

4.1.5 Simulation and results

It is to be known by now that this work adopts the synthetic turbulent inflow generation method for developing the turbulent inflow. The statistics are accumulated only after 3 flow-through times as done by (Wang et al., 2015; Touber, 2010). Consequently here, the statistics are recorded for an additional 6-flow through times after allowing the intial turbulent transient to pass. This is mainly due to the fact that the flow will be unphysical for some distance downstream of the inflow plane. In the case for a boundary layer, such physical transients are usually of the order of ten to twenty inflow-boundary-layer thickness long. Therefore it is unlikely that the phase information accommodated by such synthetic fields will match that of the real turbulence and hence this unphysical prescribed phase information will have to be allowed to adjust itself downstream of the inlet plane until it becomes physically correct. .

The figure 4.4 (as with all the cases, the flow is left to right) illustrates the contour plots of instantaneous flow properties in which the visualization of the 3D turbulent flow can be seen. The development of the boundary layer can be clearly observed. Furthermore, the arti-

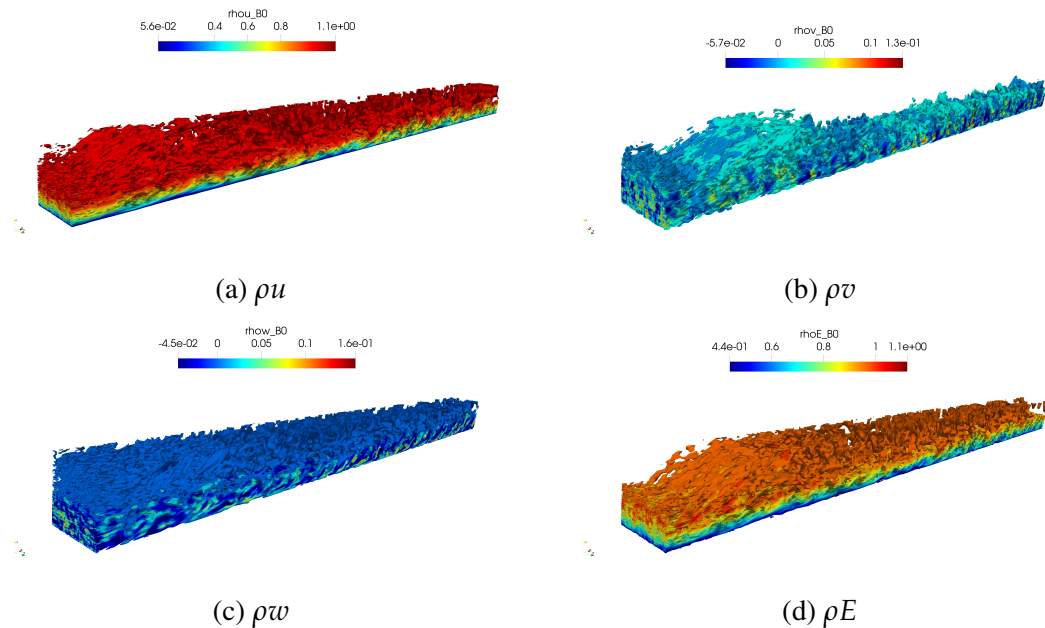


FIGURE 4.4: Contour plots of instantaneous flow properties at 9 flow-through times

ficial structures produced by the inflow method develop into larger, more coherent structures

further downstream. A considerable boundary layer growth between the inlet and exit can also be noted as shown in figure 4.5. Also, irregularities in the momentum thickness near the inlet of the domain can be observed due to formation of a weak compressible shock. Recall

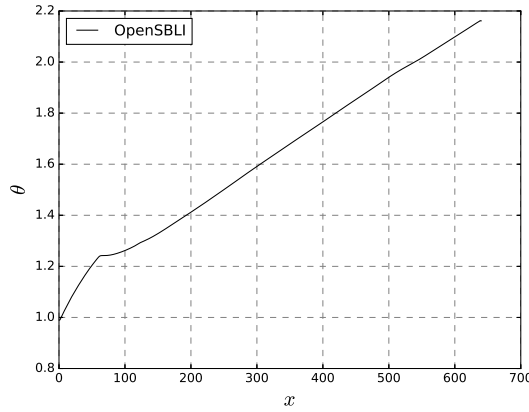


FIGURE 4.5: Momentum thickness along x

from section 3.2.1, we time average the various flow features for determining the magnitude of these flow variables as,

$$\bar{f}^t(x) = \lim_{T \rightarrow \infty} \frac{1}{T} \int_t^{t+T} f(x, t) dt \quad (4.7)$$

The figure 4.6 illustrates the time averaged mean inflow generated after the Reynolds averaging. The flow fluctuations seen in figure 4.4 can be clearly seen to be resolved into the mean

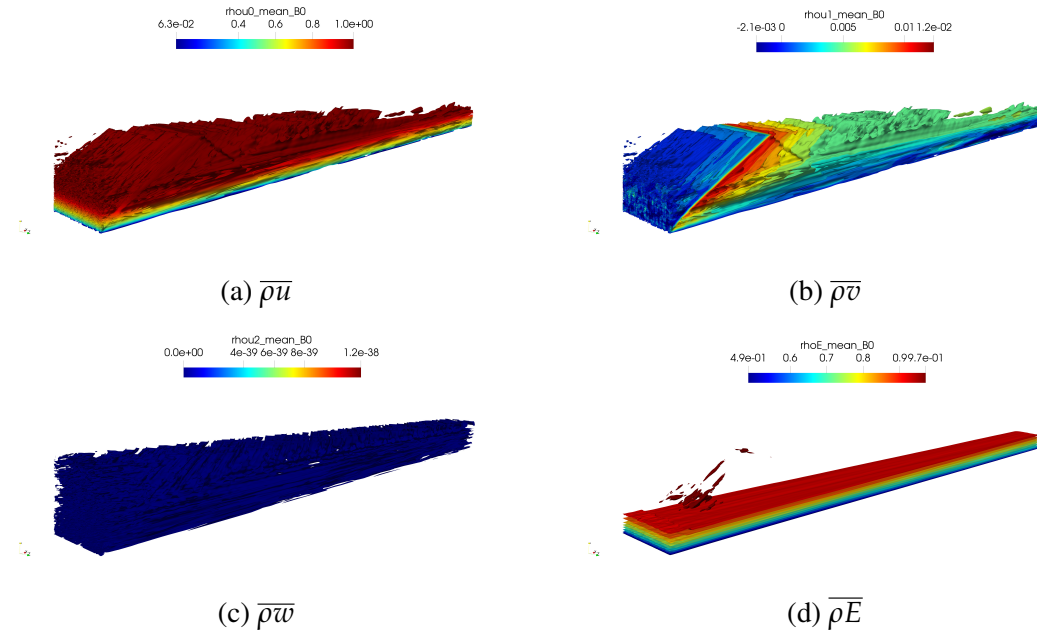


FIGURE 4.6: Contour plots of mean flow properties at 9 flow-through times

components.

Since the turbulent inflow generated is homogeneous, spatial averaging is performed for the periodic boundary condition in the z-direction. The spatial avergaing for a given time averaged function (\bar{f}) is given by,

$$(\bar{f}) = \int_0^{L_z} \bar{f}_{ij}^t dz \quad (4.8)$$

In consequence of this averaging we obtain a 2D averaged flowfield as shown in figure 4.7. Therefore, this forms the basis of the post processing. Similarly, the various spatially

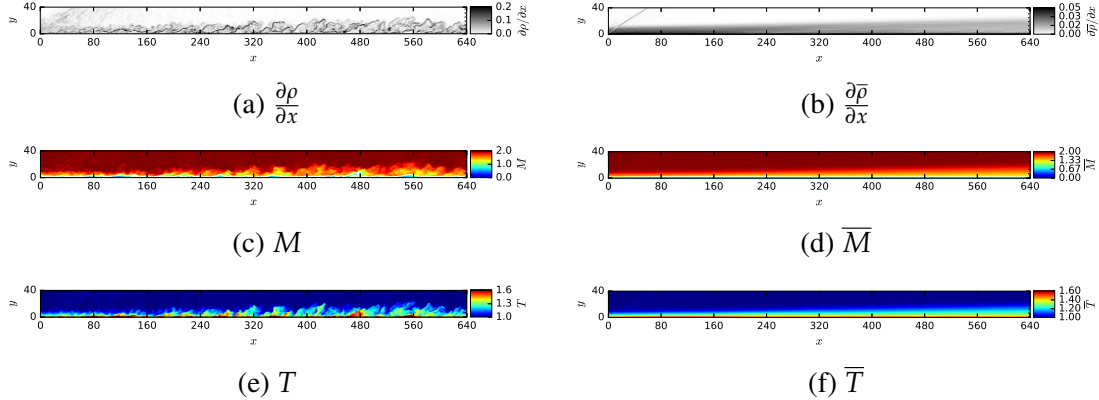


FIGURE 4.7: **Spatial averaged flow properties at 9 flow-through times**

averaged flow variables is shown in figure 4.8.

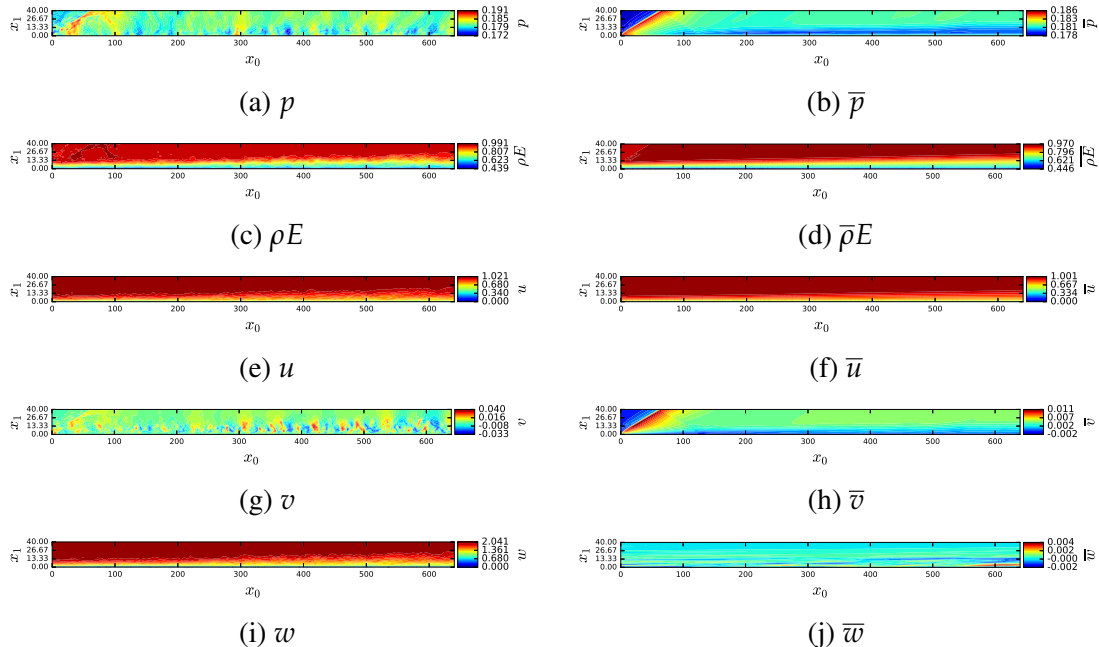


FIGURE 4.8: **Contour plots of spatial averaged flow properties at 9 flow-through times**

The first part of the validation is to assess the development of the turbulent boundary layer. This is primarily to judge the inflow turbulent boundary layer generation, however, it also provides an opportunity to consider what phenomena may be directly caused by the turbulence. This is conducted by comparing results obtained by the work of Rumsey (2015) in which, similar inflow conditions for an adiabatic bottom wall with Mach 2 have been used. Figure 4.9 illustrates the comparison performed by plotting the skin friction coefficient against the scaled Reynolds number as the skin friction provides good information about the state of the boundary layer flow very close to the wall. It is worth mentioning that the profile

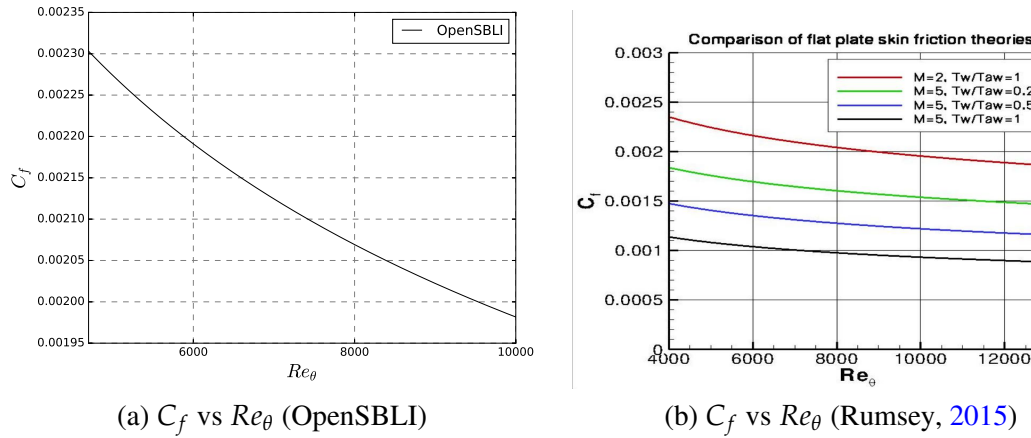


FIGURE 4.9: **Van Driest skin friction comparision**

has been Van Driest scaled (transformation described at section 3.38) to account for the high degree of compression in the boundary layer. It can be observed that the line plot obtained from the simulation matches the overall behaviour with that of the reference. However, the skin friction (C_f) acquired from the simulations differs by a few units mainly due to the difference in the wall temperature (T_{aw} / T_∞) used in this work by a factor of 0.676, compared to Rumsey (2015). Thus the observed change among the line plots is expected.

To fully validate the inflow method, it is necessary to study the boundary layer turbulence in detail. Hence, the time-averaged velocity profiles with the fitted mentioned wall function (section A.1) at a streamwise location of 500 is plotted in figure 4.10.

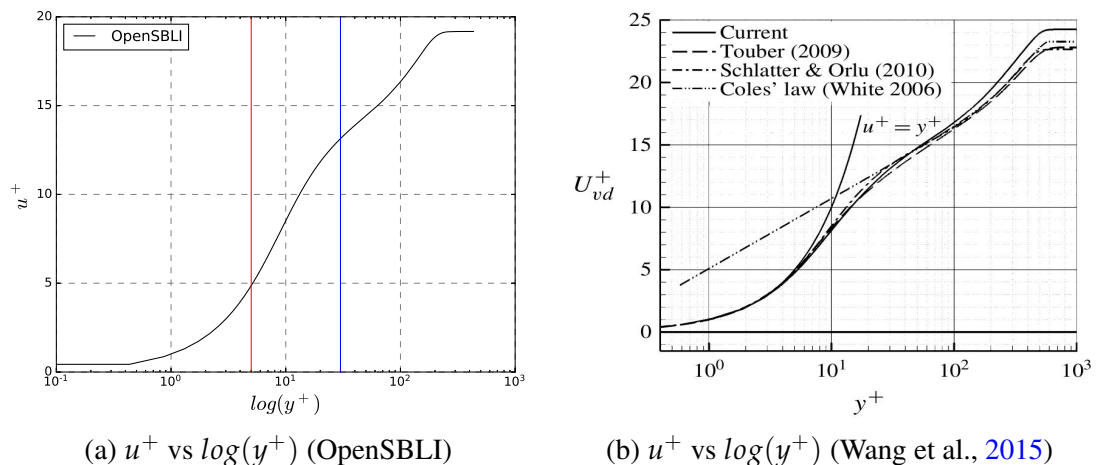


FIGURE 4.10: **Log profile near the wall**

Furthermore, to ensure that the turbulence generation method can produce a physically correct turbulent boundary layer, various time-averaged RMS flow properties are plotted in figure 4.11 which show resemblance with the reference paper (Zhang, Duan, and Choudhari, 2018). The log profile near the wall has a resemblance with the work presented by Touber

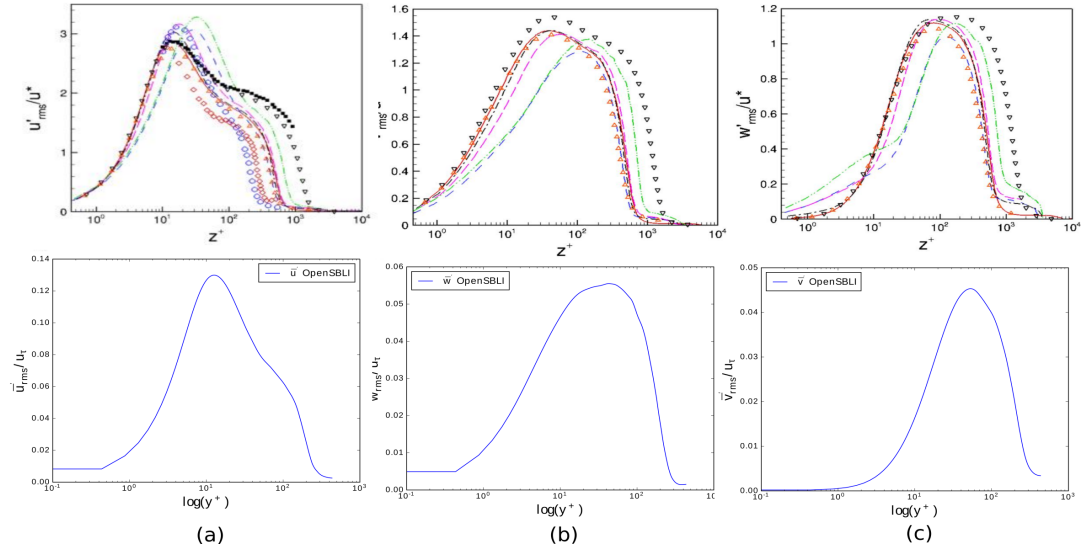


FIGURE 4.11: **Turbulence intensities**

(2010) and Wang et al. (2015) which also deals with turbulent shock wave boundary layer interactions with a higher Reynolds number ($Re = 2500, 4300$). The good convergence in the wall region suggests that the mean velocity profile is well generated and a good log law fit for this grid resolution is obtained.

4.2 Injection

4.2.1 Injection geometry and mesh

This section discusses the other half of the project where one introduces sonic jet injection in the turbulent flow field. The additional difference in the geometry from the previous section of a 3D flat plate is the inclusion of a 2×2 rectangular injection at the bottom adiabatic wall as shown in figure 4.12. The incorporation of a small injection is mainly to maintain correspondence with the conclusions drawn from the work of (Cerminara, Deiterding, and Sandham, 2018) carried out in the Cambridge University that dealt with hypersonic injections and stated the better development of thin film of fluid at low plenum pressure simulated with small slots. The injection lies at a location situated between a length of 255 to 257 and 17 to 19 in the x and z direction respectively.

The same mesh size and mesh attributes are adopted for this geometry with the same number of points in x, y and z-direction i.e. $N_x, N_y, N_z = 800, 300, 90$. Therefore, the mesh is uniformly spaced in x and z-direction with exponential stretching in y-direction as shown in figure 4.2.

4.2.2 Simulation and results

Furthermore, the inflow boundary layer turbulence is similar to the turbulent boundary layers discussed in the above section 4.1.3. It is to be noted that the simulations are as well commenced in the presence of the developed turbulent boundary layer by interpolation of

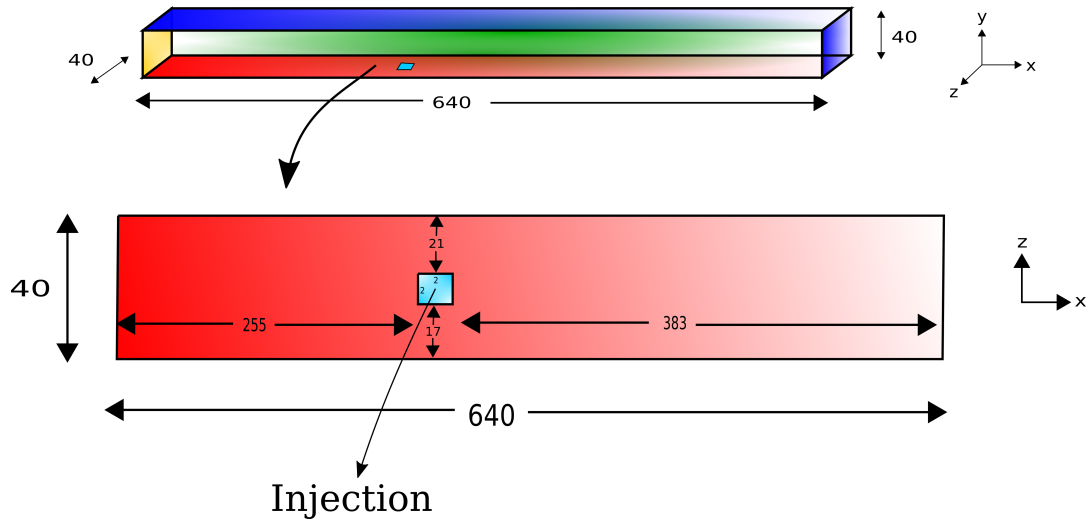
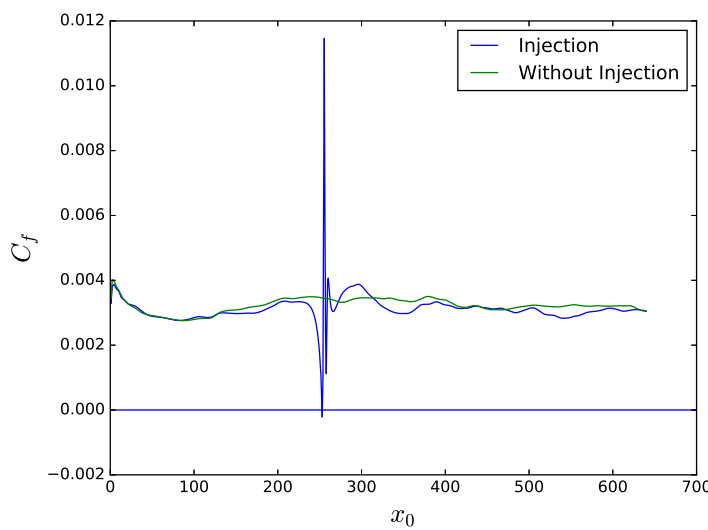


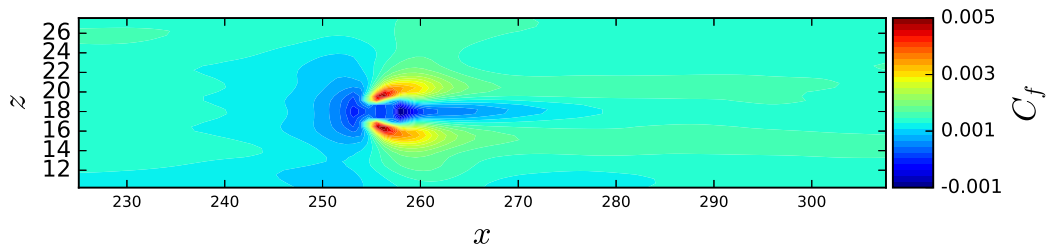
FIGURE 4.12: Schematic diagram of injection at bottom wall

the inflow from the section 4.1.2, 4.1.4. In short, prior to the 6-flow through simulations, an additional 3-flow through simulation is performed after the inclusion of the transverse injection ultimately corresponding to 3,60,000 similar to that of the simulations with flat plate geometry. Therefore, a 3D turbulent flow field is obtained along with the mixing phenomena of external fluid via the transverse injection can be observed.

It is to be expected that the introduction of the transverse flow through the injection does bring about observable changes in the flow field causing shock interactions and flow separations. The skin friction (C_f) plotted against x , is shown in figure 4.13. It can be observed that the (C_f) drops at negative values after the location of injection which suggests the phenomena of flow separation. From the figure 4.14 the generation of the complex flow

FIGURE 4.13: Skin friction line plot at $z=18$

structures due to the effect of sonic transverse injection can be observed which is further

FIGURE 4.14: Skin friction contour plot at $y=0$ plane

elaborated in section 4.2.2. The appearance of such phenomena in the flow field also reassures the effective functioning of the injection.

Figure 4.15 and 4.16 showcases the plot of various flow variables which also illustrate the same phenomena discussed.

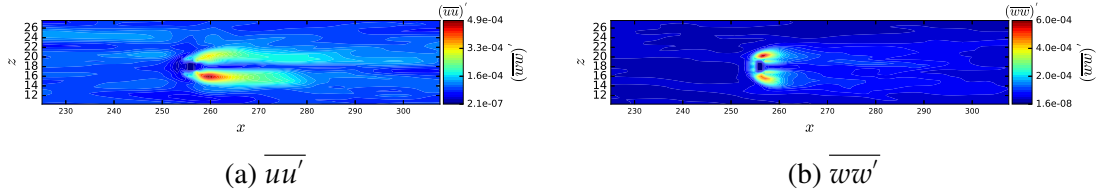


FIGURE 4.15: Contour plots streamwise and spanwise Reynolds stresses with injection at bottom wall

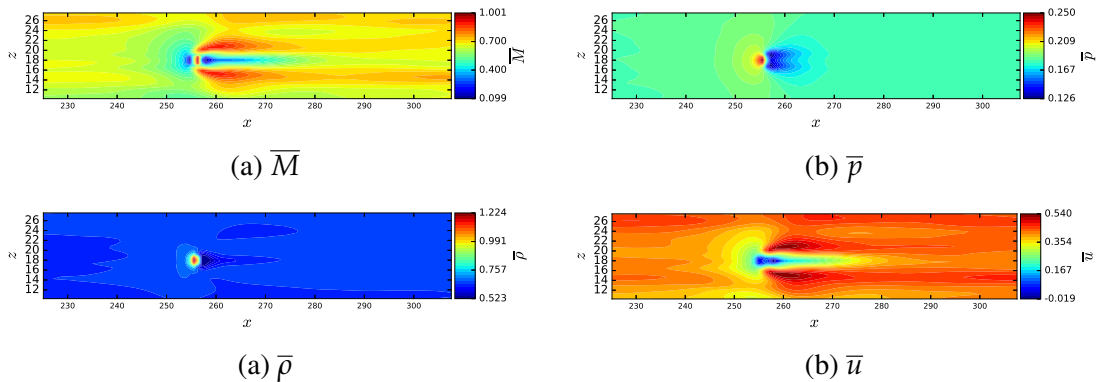


FIGURE 4.16: Contour plots of Reynolds averaged variables with injection at bottom wall

Flow features

The initial effects of the injection can be observed by the blockage of the incoming turbulent inflow normal to the injection. The various complex flow structures and shock interactions generated behind the injection is shown in figure 4.17. The turbulent fluid comes to a rest due to the presence of injection at the front that acts as an obstacle. The sudden drop of

the Mach number, as a result, generates the bow shock behind the injection. This also leads to the development of the wake region where the flow becomes laminar, having the Mach number reduced to 10^{-2} orders of magnitude. The interaction of the turned fluid with the outer boundary layer mixes with the generated shear layer behind the injection leading to formation of triple point. Furthermore, various shock to shock interactions can be observed further downstream of the domain.

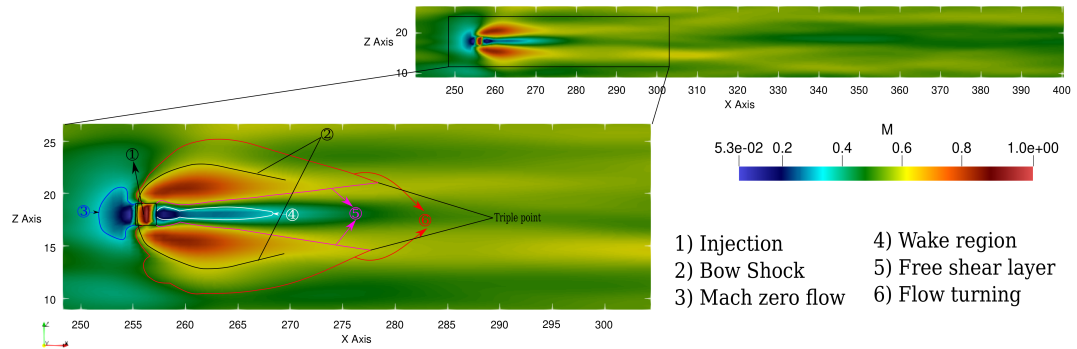


FIGURE 4.17: Complex flow structures encountered during STBLI

Chapter 5

Conslusions and future work

5.1 Conslusions

The work presented in this work can be divided into four main parts. The first part (section 4.1.3) describes the different methods and strategies adopted for developing a realistic turbulent inflow possible. The use of the digital factor approach adds a convenient solution to the relaminarization issue observed with the synthetic turbulence inflow generation method. In the second part (section 4.1.5), the time averaging of the accumulated statistics resolved the unsteadiness and fluctuations inherently built during turbulence for calculation of the flow variables. This was further averaged by applying the homogeneity of the time-averaged flow variables to the z-direction, allowing the evaluation of the fully developed turbulent boundary layer for validations. The third section (4.2) described the second half of the project in the generation of STBLIs i.e introduction of sonic injections. The fourth section (4.2.2) - analysed the core findings of this project concluding the working phenomenons of the various complex phenomena perceived in the interaction.

The summary of the major findings of this work is listed below -

- Generation of turbulent inflow via the synthetic turbulence inflow generation method.
- Calculation of the time and spatial averaged statistics.
- Validation of turbulent flow fields with the set of selected literature.
- Transverse sonic jet injection into the turbulent flow field, from the bottom wall.
- Analysis and explanation of complex flow structures identified in the STBLI.

5.2 Future work

To further investigate different aspects of the work presented in this project, some suggestions for future studies are provided in the following,

- The mesh generated in this work for the simulation can be further refined for DNS simulations and solve smaller scales of turbulence.
- The use of a bigger domain can allow us to visualize the shock to shock interactions encountered in the wake region.

Appendix A

OpenSBLI Coding Format

```

1 def wall_functions(self, rho, u, mu):
2     mu_wall = mu[0, :]
3     rho_wall = rho[0, :]
4
5     dudy = self.compute_wall_derivative(u)
6     tau_wall = dudy*mu_wall
7
8     u_tau = (tau_wall/rho_wall)**0.5
9
10    loc = 625 #500 domain length
11
12    y_plus = (self.y[:, loc] * u_tau[loc] * rho_wall[loc])/mu_wall[loc]
13    y_plus = y_plus*(self.Re)**0.5
14
15    u_plus = (u[:, loc]/u_tau[loc])*(self.Re)**0.5
16
17    return u_plus, y_plus

```

LISTING A.1: Wall Fucntions

```

1 def Re_theta(self, rhou, u):
2     re_theta = []
3     theta = []
4     for i in range(len(self.y[0,:])):
5         rho_u, u_vel = rhou[:, i], u[:, i]
6
7         limits = self.y[:, i]
8
9         yl= rho_u * (1.0 - u_vel)
10
11        ans = simps(yl, limits)
12
13        theta.append(ans)
14        re_theta.append(ans * (self.Re + 670.0)*4.0)
15
16    return re_theta, theta
17
18 def imcomp_cf(self, re_theta):
19     var = np.log10(re_theta)
20     cf_re_theta = 17.08*(var**2) + 25.11*var + 6.012
21     return (1.0/cf_re_theta)
22
23 def van_direst_Cf(self, T, re_theta, mu):
24     RefT = self.RefT
25
26     #Approximate Adibatic Wall Temperature
27     T_aw = 1.67

```

```

28
29     #Using Sutherland's Law
30     T_w = T[0,:]
31     F_re_theta = ((1.0/T_w)**(1.5)) * ((T_w*RefT + 110.4)/(RefT+110.4))
32     #F_re_theta = 1/mu[0, :] #Non Dimensionalised
33     re_theta_prime = F_re_theta*re_theta
34
35     a = ((T_aw - 1.0)/T_w)**0.5 #Non Dimensionalised
36     b = T_aw/T_w - 1.0
37     temp_var = (b**2 + 4.0*a**2)**0.5
38     A = (2.0*a**2 - b)/temp_var
39     B = b/temp_var
40
41     Fc = (T_aw - 1.0)/(np.arcsin(A) + np.arcsin(B))**2
42
43     cf_incomp = self.imcomp_cf(re_theta_prime)
44     Cf = (1.0/Fc) * cf_incomp
45     return Cf
46
47 def wall_functions(self, rho, u, mu):
48     mu_wall = mu[0, :]
49     rho_wall = rho[0, :]
50
51     dudy = self.compute_wall_derivative(u)
52     tau_wall = dudy*mu_wall
53
54     u_tau = (tau_wall/rho_wall)**0.5
55
56     loc = 625 #500 domain length
57
58     y_plus = (self.y[:, loc] * u_tau[loc] * rho_wall[loc])/mu_wall[loc]
59     y_plus = y_plus*(self.Re)**0.5
60
61     u_plus = (u[:, loc]/u_tau[loc])*(self.Re)**0.5
62
63     return u_plus, y_plus

```

LISTING A.2: Van Dirst Skin Friction

```

1 import numpy as np
2
3 # problem dimensions and coordinate symbol
4 ndim = 3
5 coordinate_symbol = "x"
6
7 Lx0 = ConstantObject('Lx0')
8 Lx1 = ConstantObject('Lx1')
9 Lx2 = ConstantObject('Lx2')
10 CTD.add_constant([Lx0, Lx1, Lx2])
11
12 # Create SimulationEquations and Constituent relations, add the expanded
13 # equations
14 metriceq = MetricsEquation()
15 metriceq.generate_transformations(ndim, coordinate_symbol, [(False, False),
16                         (True, False), (False, False)], 2)
17
18 # variable dictionaries
19 local_dict = {"block": block, "GridVariable": GridVariable, "DataObject": DataObject}
20 local_dict['by'], local_dict['bz'] = ConstantObject('by'), ConstantObject('bz')

```

```
19 local_dict['block0np0'], local_dict['block0np1'], local_dict['block0np2']  
    = ConstantObject('block0np0'), ConstantObject('block0np1'),  
    ConstantObject('block0np2')  
20  
21 # grid equations  
22 x0 = parse_expr("Eq(DataObject(x0), block.deltas[0]*block.grid_indexes[0])  
    ", local_dict=local_dict)  
23 x1 = parse_expr("Eq(DataObject(x1), Lx1*sinh(by*block.deltas[1]*block.  
    grid_indexes[1]/Lx1)/sinh(by))", local_dict=local_dict)  
24 x2 = parse_expr("Eq(DataObject(x2), block.deltas[2]*block.grid_indexes[2])  
    ", local_dict=local_dict)  
25  
26 # set grid initialisation  
27 initial = GridBasedInitialisation()  
28 initial_eqns = [x0, x1, x2]  
29 initial.add_equations(initial_eqns)
```

LISTING A.3: **Grid generation**

Bibliography

- [1] Holger Babinsky and John K Harvey. *Shock wave-boundary-layer interactions*. Vol. 32. Cambridge University Press, 2011.
- [2] T. Buffin-Bélanger, A.G. Roy, and S. Demers. “9.6 Turbulence in River Flows”. In: *Treatise on Geomorphology*. Ed. by John F. Shroder. San Diego: Academic Press, 2013, pp. 69–86. ISBN: 978-0-08-088522-3.
- [3] Adriano Cerminara, Ralf Deiterding, and Neil Sandham. “Direct numerical simulation of blowing in a hypersonic boundary layer on a flat plate with slots”. In: *2018 Fluid Dynamics Conference*. 2018, p. 3713.
- [4] Jean Cousteix. “Aircraft Aerodynamic Boundary Layers”. In: *Encyclopedia of Physical Science and Technology (Third Edition)*. Ed. by Robert A. Meyers. Third Edition. New York: Academic Press, 2003, pp. 301–317. ISBN: 978-0-12-227410-7.
- [5] Nicholas J DiGregorio, Tomasz G Drozda, and Cyrus K Madnia. “Comparison of Boundary Layer Similarity Transformations for High Mach Number Flows”. In: *AIAA Scitech 2019 Forum*. 2019, p. 1390.
- [6] David S Dolling. “Fifty years of shock-wave/boundary-layer interaction research: what next?” In: *AIAA journal* 39.8 (2001), pp. 1517–1531.
- [7] Dimitris Drikakis. “Advances in turbulent flow computations using high-resolution methods”. In: *Progress in Aerospace Sciences* 39.6-7 (2003), pp. 405–424.
- [8] Lin Fu, Xiangyu Y Hu, and Nikolaus A Adams. “A family of high-order targeted ENO schemes for compressible-fluid simulations”. In: *Journal of Computational Physics* 305 (2016), pp. 333–359.
- [9] Lin Fu, Xiangyu Y Hu, and Nikolaus A Adams. “Improved five-and six-point targeted essentially nonoscillatory schemes with adaptive dissipation”. In: *AIAA Journal* 57.3 (2019), pp. 1143–1158.
- [10] PC Huang, GN Coleman, and P Bradshaw. “Compressible turbulent channel flows: DNS results and modelling”. In: *Journal of Fluid Mechanics* 305 (1995), pp. 185–218.
- [11] PG Huang and Gary N Coleman. “Van Driest transformation and compressible wall-bounded flows”. In: *AIAA journal* 32.10 (1994), pp. 2110–2113.
- [12] Christian T Jacobs, Satya P Jammy, and Neil D Sandham. “OpenSBLI: A framework for the automated derivation and parallel execution of finite difference solvers on a range of computer architectures”. In: *Journal of Computational Science* 18 (2017), pp. 12–23.
- [13] Satya P Jammy, Gihan R Mudalige, Istvan Z Reguly, Neil D Sandham, and Mike Giles. “Block-structured compressible Navier–Stokes solution using the OPS high-level abstraction”. In: *International Journal of Computational Fluid Dynamics* 30.6 (2016), pp. 450–454.
- [14] Guang-Shan Jiang and Chi-Wang Shu. “Efficient implementation of weighted ENO schemes”. In: *Journal of computational physics* 126.1 (1996), pp. 202–228.

- [15] Bibin John. "Numerical Investigations of Shock Wave Boundary Layer Interaction in Hypersonic Flows". PhD thesis. 2014.
- [16] Eric Johnsen, Johan Larsson, Ankit V Bhagatwala, William H Cabot, Parviz Moin, Britton J Olson, Pradeep S Rawat, Santhosh K Shankar, Björn Sjögren, Helen C Yee, et al. "Assessment of high-resolution methods for numerical simulations of compressible turbulence with shock waves". In: *Journal of Computational Physics* 229.4 (2010), pp. 1213–1237.
- [17] E. Katzer. "On the lengthscales of laminar shock/boundary-layer interaction". In: *Journal of Fluid Mechanics* 206 (Sept. 1989), pp. 477–496. DOI: [10.1017/S0022112089002375](https://doi.org/10.1017/S0022112089002375).
- [18] Markus Klein, Amsini Sadiki, and Johannes Janicka. "A digital filter based generation of inflow data for spatially developing direct numerical or large eddy simulations". In: *Journal of computational Physics* 186.2 (2003), pp. 652–665.
- [19] Sang-Hyeon Lee, In-Seuck Jeung, and Youngbin Yoon. "Computational investigation of shock-enhanced mixing and combustion". In: *AIAA journal* 35.12 (1997), pp. 1813–1820.
- [20] David Lusher. "Shock-wave/boundary-layer interactions with sidewall effects in the OpenSBLI code-generation framework". PhD thesis. University of Southampton, 2020.
- [21] David J Lusher, Satya P Jammy, and Neil D Sandham. "OpenSBLI: Automated code-generation for heterogeneous computing architectures applied to compressible fluid dynamics on structured grids". In: *arXiv preprint arXiv:2007.14933* (2020).
- [22] David J Lusher, Satya P Jammy, and Neil D Sandham. "Shock-wave/boundary-layer interactions in the automatic source-code generation framework OpenSBLI". In: *Computers & Fluids* 173 (2018), pp. 17–21.
- [23] V Mali and S Dange. "Basics of Y Plus, Boundary Layer and Wall Function in Turbulent Flows". In: *Learncax*, [Online]. Available: <https://www.learncax.com/knowledge-base/blog/bycategory/cfd/basics-of-y-plus-boundary-layer-and-wall-function-in-turbulent-flows>. [Accessed 19 Oct. 2015] (2010).
- [24] Len G Margolin, William J Rider, and Fernando F Grinstein. "Modeling turbulent flow with implicit LES". In: *Journal of Turbulence* 7 (2006), N15.
- [25] A Misra. "Composite materials for aerospace propulsion related to air and space transportation". In: *Lightweight Composite Structures in Transport*. Elsevier, 2016, pp. 305–327.
- [26] Jens M Österlund. "Experimental studies of zero pressure-gradient turbulent boundary layer flow". PhD thesis. Mekanik, 1999.
- [27] Sergio Pirozzoli. "Numerical Methods for High-Speed Flows". In: *Annual Review of Fluid Mechanics* 43.1 (2011), pp. 163–194. DOI: [10.1146/annurev-fluid-122109-160718](https://doi.org/10.1146/annurev-fluid-122109-160718).
- [28] Stephen B Pope. *Turbulent flows*. 2001.
- [29] Konstantinos Ritos, Ioannis W Kokkinakis, and Dimitris Drikakis. "Physical insight into a mach 7.2 compression corner flow". In: *2018 AIAA Aerospace Sciences Meeting*. 2018, p. 1810.
- [30] Christopher L Rumsey. "Recent developments on the turbulence modeling resource website". In: *22nd AIAA Computational Fluid Dynamics Conference*. 2015, p. 2927.
- [31] N. D. Sandham. "Shock Wave – Boundary Layer Interactions H. Babinsky and J. K. Harvey Cambridge University Press, Cambridge, UK. 2011. 461pp. Illustrated. £80. ISBN 978-0-521-84852-7." In: *The Aeronautical Journal* (1968) 117.1192 (2013), 649–649. DOI: [10.1017/S0001924000008277](https://doi.org/10.1017/S0001924000008277).

- [32] ND Sandham, YF Yao, and AA Lawal. “Large-eddy simulation of transonic turbulent flow over a bump”. In: *International Journal of Heat and Fluid Flow* 24.4 (2003), pp. 584–595.
- [33] Andrea Sansica, Neil Sandham, and Zhiwei Hu. “Stability and unsteadiness in a 2D laminar shock-induced separation bubble”. In: *43rd AIAA Fluid Dynamics Conference*. 2013, p. 2982.
- [34] Philipp Schlatter and Ramis Örlü. “Assessment of direct numerical simulation data of turbulent boundary layers”. In: *Journal of Fluid Mechanics* 659 (2010), p. 116.
- [35] Karl Ernest Schoenherr. “Resistance of flat surfaces moving through a fluid”. In: *Trans. Soc. Nav. Archit. Mar. Eng.* 40 (1932), pp. 279–313.
- [36] Vatsalya Sharma, Vinayak Eswaran, and Debasis Chakraborty. “Computational analysis of transverse sonic injection in supersonic crossflow using rans models”. In: *Journal of Fluids Engineering* 142.6 (2020).
- [37] Vatsalya Sharma, Vinayak Eswaran, and Debasis Chakraborty. “Effect of fuel-jet injection angle variation on the overall performance of a SCRAMJET engine”. In: *Aerospace Science and Technology* 100 (2020), p. 105786.
- [38] DB Spalding and SW Chi. “The drag of a compressible turbulent boundary layer on a smooth flat plate with and without heat transfer”. In: *Journal of Fluid Mechanics* 18.1 (1964), pp. 117–143.
- [39] LEAP CFD Team et al. “turbulence part 3-selection of wall functions and $y+$ to best capture the turbulent boundary layer”. In: *Consulted on* 7.05 (2013), p. 2015.
- [40] C Tenaud, E Garnier, and P Sagaut. “Evaluation of some high-order shock capturing schemes for direct numerical simulation of unsteady two-dimensional free flows”. In: *International Journal for Numerical Methods in Fluids* 33.2 (2000), pp. 249–278.
- [41] VT Ton, AR Karagozian, FE Marble, SJ Osher, and BE Engquist. “Numerical simulations of high-speed chemically reacting flow”. In: *Theoretical and Computational Fluid Dynamics* 6.2 (1994), pp. 161–179.
- [42] Emile Touber. “Unsteadiness in shock-wave/boundary layer interactions”. PhD thesis. University of Southampton, 2010.
- [43] Bo Wang, Neil D Sandham, Zhiwei Hu, and Weidong Liu. “Numerical study of oblique shock-wave/boundary-layer interaction considering sidewall effects”. In: *Journal of Fluid Mechanics* 767 (2015), pp. 526–561.
- [44] Frank M White and Isla Corfield. *Viscous fluid flow*. Vol. 3. McGraw-Hill New York, 2006.
- [45] David C Wilcox. “Turbulence modeling for CFD. La Canada, CA: DCW Industries”. In: *Inc, November* (2006).
- [46] Minwei Wu and M Pino Martin. “Analysis of shock motion in shockwave and turbulent boundary layer interaction using direct numerical simulation data”. In: *Journal of Fluid Mechanics* 594 (2008), p. 71.
- [47] Chao Zhang, Lian Duan, and Meelan M Choudhari. “Direct numerical simulation database for supersonic and hypersonic turbulent boundary layers”. In: *AIAA Journal* 56.11 (2018), pp. 4297–4311.